Ocean Engineering 283 (2023) 115094

Contents lists available at ScienceDirect

Ocean Engineering

journal homepage: www.elsevier.com/locate/oceaneng

Hydrodynamic characteristics of a 15 MW semi-submersible floating offshore wind turbine in freak waves

Wenjie Zhong [a], Xiaoming Zhang [b], Decheng Wan [a,*]

[a] Computational Marine Hydrodynamics Lab (CMHL), School of Naval Architecture, Ocean and Civil Engineering, Shanghai Jiao Tong University, Shanghai, China
[b] Zhongnan Engineering Corporation Limited, Changsha, China

ARTICLE INFO

Keywords:
Floating offshore wind turbine
Computational fluid dynamics
Freak wave
Wave-structure interaction
Mooring dynamics

ABSTRACT

Dynamics of the floating offshore wind turbines (FOWTs) in harsh ocean environments gains increasing attention due to the high maintenance costs in case of structural damage. The freak wave occurring more frequently than believed poses a threat to FOWTs, but mechanism and influencing factors of the wave-structure interaction problem have not been fully explained. In this paper, dynamics of the VolturnUS-S semi-submersible platform designed for the IEA 15 MW wind turbine under freak waves is studied using a coupled computational fluid dynamics and finite element mooring line model. First, the hydrodynamic model is validated using the DeepCwind semi-submersible platform. Then, the validated model is employed for the analysis of the VolturnUS-S semi-submersible platform under freak waves described as a focused group of waves. Hydrodynamic behaviors of the semi-submersible FOWT are described in detail, and parametric analysis of the problem including the effects of focusing crest amplitude, focusing location, incident angle, gravity center location is conducted. Important results include the dramatic surge motion of the platform and fairlead tension of the upstream mooring line, and alleviation of these responses by varying the wave angle to 30° and moving the gravity center to the centroid of the platform geometry.

1. Introduction

The advancement of floating offshore wind turbines (FOWTs) along with the exploration of offshore wind energy has been ocean engineering trends for decades due to the demands for clean and renewable energies. FOWTs are designed to be deployed in deep waters where more stable wind resources abound in comparison to onshore and nearshore sites, and have become one of the research focuses in the wind energy community. One of the challenges faced by the FOWT practitioners is the accurate evaluation of dynamics of the complete floating system under wind and wave conditions. The FOWT is a multi-body system consisting of the wind turbine, the control sector, the tower, the floating platform for supporting the upper structure and the mooring system for restricting the drift motion (Liu et al., 2016). The aerodynamics of the wind turbine is affected by the motions of the supporting platform in six degrees of freedom (DOFs), having greater uncertainties in power production and higher fatigue failure probability of the blades (Liu et al., 2019; Tran and Kim, 2016a). On the contrary, the hydrodynamics of the platform is modified due to the wind-induced constant inclination and variational pitching motion (Antonutti et al., 2016). The addition of the mooring systems further complicates the coupled effects between different components of the FOWTs (Hall et al., 2014).

Methods for assessing the coupled dynamics of FOWTs generally fall into two classes. One is based on engineering models and the other is based on the computational fluid dynamics (CFD). The model-based approach uses empirical formula for the aerodynamic and hydrodynamic loads, and possesses the feature of fast computation which is suitable for the preliminary design purpose (Dai et al., 2018; Jonkman, 2009; Robertson et al., 2014). One well-known model-based code is the open source FAST which can conduct fully coupled time-domain aero-hydro-servo-elastic analysis of FOWT systems. FAST adopts the blade element momentum (BEM) method with various empirical and semi-empirical correction models for the aerodynamics and the potential flow theory augmented with the quadratic damping from Morison's equation for the hydrodynamics. Both loading models are low order with simplification assumptions. While the low order models in aerodynamics and hydrodynamics affect the overall accuracy and range of application of the model-based approach, the structural dynamics can be directly obtained which can be used for ultimate and fatigue load evaluations (Kvittem and Moan, 2015; Luan et al., 2017). The CFD

* Corresponding author.
E-mail address: dcwan@sjtu.edu.cn (D. Wan).

https://doi.org/10.1016/j.oceaneng.2023.115094
Received 14 February 2023; Received in revised form 8 May 2023; Accepted 10 June 2023
Available online 21 June 2023

approach has long been applied in simulating FOWTs (Cheng et al., 2019; Huang et al., 2019; Liu et al., 2017; Tran and Kim, 2015, 2016b; Yan et al., 2016). In contrast to the model-based approach, real flow is inherently considered in CFD so that aerodynamic and hydrodynamic loadings can be well predicted by integration of pressure and viscous stress with the accuracy dependent on the fidelity of the numerical schemes. Particularly for the wave-structure interaction problems, wave breaking and run-up, vortex generation and shedding are inherently included in the nonlinear equations. Full-scale modeling of FOWT systems is possible with CFD, and thus concerns on the scaling effects can be put aside. It is to note that as the structures are treated as boundaries in CFD, fluid-structure interaction simulations of FOWTs can be realized with external codes to account for the flexibility of the structure (Carrion et al., 2014; Lee et al., 2017; Liu et al., 2019). With the above-mentioned advantages, there is a rising number of researchers to choose CFD as the tool for FOWT analyses.

For CFD analyses of FOWTs, one challenge is to incorporate the role of mooring systems. Plenty of researches used the quasi-static model for either hydrodynamic-mooring (Lin et al., 2021; Huang et al., 2021; Tran and Kim, 2015) or aerodynamic-hydrodynamic-mooring (Cheng et al., 2019; Liu et al., 2017; Liu et al., 2019; Tran and Kim, 2016b) analysis. The quasi-static model solves for the mooring line profile and tension analytically with the assumption that the line is in static equilibrium. The hydrodynamic and inertial forces are neglected in the model which affects the prediction of the motion response of the moored structure and the mooring loads. Studies showed that the use of dynamic models is in many cases necessary for accurately predicting mooring line loads, which is crucial for designing the mooring system and assessing the FOWT dynamics. Masciola et al. (2013) compared the response of the DeepCwind semi-submersible platform in coupled simulations using the quasi-static mooring model MAP and the finite element model OrcaFlex against 1:50 scale test, and found that the platform motions are influenced by mooring dynamics only in extreme sea states but the mooring dynamics is important to the mooring line tensions in all load cases. Hall et al. (2014) compared quasi-static and finite element mooring models across three classes of floating platform designs and reached similar conclusions as Masciola et al. (2013). Thus, a CFD model that incorporates mooring line dynamics is essential for the thorough understanding of FOWTs' coupling behaviors. To the authors' knowledge, among the four types of dynamic mooring models, i.e., lumped mass (LM) method, finite element method (FEM), finite difference method (FDM) and multi-body dynamics (MBD) method, only the LM method has been used in the coupled CFD simulations of FOWTs (Li et al., 2019; Zhou et al., 2019). A FDM mooring dynamics model was developed by Chen et al. (2018) and has been used for the model-based analysis of FOWTs. In Antonutti et al. (2018), the open source FEM code_Aster was applied for the dynamic mooring modeling in the model-based FOWT analysis. It is found that the FEM dynamic mooring model has been scarcely used in the coupled CFD-mooring simulations of FOWTs.

The dynamics of FOWT systems under freak waves receives rising attentions due to the high maintenance costs in case of structural damage. The freak wave which appears as "walls of water", "holes in the sea" or several successive high waves (three sisters) is defined as having a height that exceeds twice the significant wave height, and can induce large and unpredictable hydrodynamic loadings and damages to marine structures (Roy et al., 2017). It was reported that 22 supercarriers got lost after collisions with freak waves from 1969 to 1994 (Dysthe et al., 2008). Offshore platforms are also vulnerable to freak waves. The Draupner jacket platform in the North Sea confronted the famous New Year Wave on January 1, 1995 which was measured at 25.6 m crest to trough while the significant height was only 11.92 m (Clauss, 2002). Reports on the terrible damage caused by freak waves urge that a consideration of freak wave attacks at the design stage of marine structures is indispensable (Bertotti and Cavaleri, 2008). Moreover, the Maxwave project of the European Space Agency observed more than 10 giant waves over 25 m high in three weeks, showing that they are a real danger to shipping and offshore industries and occur more frequently than commonly believed (Lehner and Rosenthal, 2006).

There have been some explorations of freak wave impacts on offshore structures to reveal the mechanism and influencing factors of the nonlinear wave-structure interaction problem. Chandrasekaran and Yuvraj (2013) simulated the dynamics of a tension leg platform (TLP) in freak waves, and found that the heave excitation is significant and the motion responses are sensitive to wave directions. Zhao and Hu (2012) conducted both simulations and experiments of a two-dimensional floating object under focused wave conditions, and indicated that the peak roll and heave motions are affected by the object's spatial relation to the wave focusing position. Deng et al. (2014) studied the effects of freak waves on a semi-submersible platform and found dramatic responses in the surge motion. This large displacement in surge under extreme waves can result in high tensions in mooring lines. An example of accident in this type is the mooring lines of a semi-submersible platform being exposed to a harsh storm in the North Sea were damaged in December 1990 (Yilmaz and Incecik, 1996). A study on the extraordinary surge responses of a semi-submersible platform interacting with the New Year Wave was conducted by Deng et al. (2017), and sensitivity analysis on the effects of relative phase, crest amplitude and three sister waves revealed that further enlargement in surge motion amplitude is obtained in cases of in-phase freak wave action, rise in crest amplitude and three sister waves. The study of Cleary and Rudman (2009) considered the effect of wave height on the normal wave impacting a semi-submersible platform with two different mooring configurations, i.e., a TLP and one with a taut spread mooring (TSM) system with untensioned lines making a 45° angle with the seabed. It was found that the heave and surge responses of the two mooring systems are expressively different with large heave and small surge for the TLP and vice versa for the TSM system. Rudman and Cleary (2013) studied the nonlinear dynamic problem of a large breaking wave on a semi-submersible TLP using the smoothed particle hydrodynamics (SPH) approach and analyzed the effects of wave impact angle and mooring line pretension. They found that the effect of wave impact angle is to determine the peak tension and slackness of the mooring lines, and a 45° impact causes the maximum tension in the leading line. In contrast, the maximum responses in surge, heave and pitch vary slightly with the wave impact angle. Rudman and Cleary (2013) also found that with raised pretension, the peak mooring line tension increases slightly but the incidence of mooring line slack status decreases significantly. In a subsequent study, Rudman and Cleary (2016) focused on the effects that the mooring systems with different choices of configuration and line composition exert on the semi-submersible platform dynamics in rogue waves. Four mooring systems including the initial TLP and TSM and two hybrids of them were considered. SPH results revealed that both the hybrid mooring systems have advantages over the nonhybrid ones, and the use of polyester ropes in the diagonal mooring lines of one hybrid mooring system offers advantages in platform responses. Zhou et al. (2019) examined the wave-wind-structure interaction of both fixed and floating semi-submersible platforms mounted by a parked NREL 5 MW wind turbine in severe sea states. Simulation results showed increased nonlinearity in motion responses and hydrodynamic loadings of the platform with the wave steepness, and more violent platform dynamics in a focused wave event than that under a regular wave impact.

Through the above review, it is realized that a detailed description of the dynamics of the widely adopted catenary moored semi-submersible platform designed for FOWTs under freak waves has not been reported. Besides, a parametric analysis on this wave-structure interaction problem is lacking in literature. Thus, in the present paper, dynamics of the UMaine VolturnUS-S semi-submersible platform designed for supporting the IEA 15 MW wind turbine under freak waves is numerically studied (Allen et al., 2020; Gaertner et al., 2020). As the impact of freak waves on a floating offshore structure is highly nonlinear in terms of hydrodynamic responses of the floating platform and tension loads in the mooring system, a high order numerical method is required. In this

study, a fully coupled CFD and dynamic mooring model for FOWT hydrodynamics is presented and validated against published experimental and numerical data. The adopted mooring solver is an in-house FEM code which uses the local discontinuous Galerkin (LDG) method of arbitrary spatial order to simulate flexible cables with no bending and torsional stiffness (Palm et al., 2017). The LDG formulation allows the solution to be discontinuous over elemental boundaries which are related by numerical fluxes and is argued to be better suited for handling shock waves (such as snap loads) than conventional discretization approaches. The DeepCwind FOWT semi-submersible platform is used for the validation purpose (Coulling et al., 2013; Koo et al., 2014). The free-decay tests and motion responses in regular waves of the platform are conducted to confirm the effectiveness of the coupled CFD and mooring model. The validated hydrodynamic-mooring model is then utilized for the dynamic analysis of the UMaine VolturnUS-S semi--submersible platform under freak waves (Allen et al., 2020). The freak wave is described by a focused group of waves derived from the JONSWAP spectrum. Extensive parametric analysis of the hydrodynamic properties of the 15 MW semi-submersible FOWT including the effects of focusing crest amplitude, focusing location, incident angle and gravity center location is conducted to provide a thorough understanding of this wave-structure interaction problem.

The remainder of the paper is organized as follows. The viscous flow model including the rigid body dynamics and the mesh deformation is given in the next section. Details of the LDG FEM dynamic mooring line model and its coupling to CFD are presented in section 3. The freak wave generation and active wave absorption in CFD framework are described in section 4. Then in section 5, the CFD-mooring and freak wave generation models are validated. Computational details regarding the physical model of the UMaine VolturnUS-S semi-submersible platform and the numerical setup are presented in section 6. In section 7, parametric analysis results on the hydrodynamics of the platform under the impact of freak waves are discussed. Finally, the conclusions are made in section 8.

2. Viscous flow model

2.1. Governing equations

For studying the hydrodynamics of semi-submersibles in extreme waves, two approaches have been used, i.e., the mesh free smoothed particle hydrodynamics (SPH) technique (Rudman and Cleary, 2013, 2016) and the mesh-based CFD (Zhou et al., 2019). Results from Rudman and Cleary (2013, 2016) showed how the SPH can be used for wave-structure interaction problems and platform design, providing an effective technique for non-linear situations. In the present study, the mesh-based CFD is used.

For viscous and incompressible two-phase flows, the continuity and Navier-Stokes (N–S) equations forcing the conservations of mass and momentum are applied as

$$\nabla \cdot \boldsymbol{u} = 0 \tag{1}$$

$$\frac{\partial \rho \boldsymbol{u}}{\partial t} + \nabla \cdot \{\rho(\boldsymbol{u} - \boldsymbol{u}_g)\boldsymbol{u}\} = -\nabla p_d - \boldsymbol{g} \cdot \boldsymbol{x} \nabla \rho + \nabla \cdot \{(\mu + \mu_t)(\nabla \boldsymbol{u} + (\nabla \boldsymbol{u})^T)\} + \sigma \kappa \nabla \alpha \tag{2}$$

where $\boldsymbol{u}$ and p are the velocity and pressure of the flow, respectively. $\boldsymbol{u_g}$ is the velocity of grid points. A dynamic pressure p_d defined as $p_d = p - \rho \boldsymbol{g} \cdot \boldsymbol{x}$ is used in the momentum equation (2) to simplify the definition of pressure condition at wall boundaries where the normal gradient of pressure for the air and water phases may be different due to the hydrostatic effect (Berberovic et al., 2009). μ and μ_t are the molecular and turbulent eddy viscosity, respectively. The turbulent eddy viscosity is obtained by the Mentor SST k - ω model via solving two extra equations, i.e., transport equations of the turbulent kinetic energy k and the specific turbulence dissipation ω. The use of the Mentor SST k - ω model is based on the knowledge from the previous studies of the authors, e.g., Zhong et al. (2020a, 2020b), and the literature (Moukalled et al., 2015), which indicated that the Mentor SST k-ω model has better adverse pressure gradient performance than other eddy-viscosity models. Moreover, the two-equation k-ω turbulence model has also been used in the wave-structure interaction simulations in Ong et al. (2017).

$$\frac{\partial(\rho k)}{\partial t} + \nabla \cdot (\rho \boldsymbol{u} k) = \nabla \cdot \left\{ \left(\mu + \frac{\mu_t}{\widetilde{\sigma}_k} \right) \nabla k \right\} + \widetilde{P}_k - 0.09 \rho k \omega \tag{3}$$

$$\frac{\partial(\rho \omega)}{\partial t} + \nabla \cdot (\rho \boldsymbol{u} \omega) = \nabla \cdot \left\{ \left(\mu + \frac{\mu_t}{\widetilde{\sigma}_\omega} \right) \nabla \omega \right\} + \widetilde{C}_\alpha \frac{\omega}{k} P_k - \widetilde{C}_\beta \rho \omega^2 + 2(1 - F_1)\sigma_{\omega 2} \frac{\rho}{\omega} \nabla k \cdot \nabla \omega \tag{4}$$

$$\mu_t = \frac{0.31 \rho k}{\mathrm{Max}\left[0.31\omega, \sqrt{2} S_r F_2\right]} \tag{5}$$

where $\widetilde{P}_k$ is the production of turbulent kinetic energy. The constants in equations (3) and (4) depend on the blending function F_1 in the form $\widetilde{\varphi} = F_1 \varphi_1 + (1 - F_1)\varphi_2$, where φ_1 and φ_2 are the corresponding constants in the original k - ω and k - ε models respectively. The constants of the original models are assigned the following values: $C_{\alpha 1} = 0.5532$, $C_{\beta 1} = 0.075$, $\beta^* = 0.09$, $\sigma_{k1} = 2.00$, $\sigma_{\omega 1} = 2.00$, $C_{\alpha 2} = 0.4403$, $C_{\beta 2} = 0.0828$, $\sigma_{k2} = 1.00$ and $\sigma_{\omega 2} = 1.186$. The use of equation (5) to calculate the turbulent eddy viscosity is favorable as it guarantees that Bradshow's assumption is satisfied (Moukalled et al., 2015).

Pressure gradient due to surface tension at the water surface is accounted for by the fourth term on the right-hand side of equation (2). The air-water interface is captured with the volume of fluid (VOF) model (Hirt and Nichols, 1981). In VOF, the surface construction is realized through the volume fraction which varies between 0 and 1 depending on the percentage of water phase in the cell volume. A water cell is marked by $\alpha = 1$, an air cell is marked by $\alpha = 0$, and the air-water interface is presented where $0 < \alpha < 1$. The advection equation of the volume fraction is given as

$$\frac{\partial \alpha}{\partial t} + \nabla \cdot (\boldsymbol{u}\alpha) + \nabla \cdot [\boldsymbol{u_r} \alpha (1 - \alpha)] = 0 \tag{6}$$

where the third term on the left-hand side is an artificial compression used for sharpening the interface (Berberovic et al., 2009). $\boldsymbol{u_r}$ is the compression velocity defined as the relative velocity between water and air. In order that the compression acts in the direction perpendicular to the water surface, the compression velocity is a function of the gradient of volume fraction. With the introduction of volume fraction, the fluid properties at a cell are evaluated by the weighted average, e.g., $\rho = \alpha \rho_{water} + (1 - \alpha)\rho_{air}$. Are solved sequentially in the numerical time stepping using the finite volume method (FVM). The FVM is implemented by integrating each term in the equations over a control volume and relating the volume integrals to the surface integrals using Gauss's theorem. The surface and volume integrals are both treated with the mid-point integration approximation which yields second order accuracy. The convective and diffusive fluxes at cell faces are evaluated with second order upwind and central differencing schemes, respectively. The Euler scheme is used for time integration. The transport equation of the volume fraction is solved with the multidimensional universal limiter for explicit solution (MULES) (Rusche, 2003).

The multiphase solver in OpenFOAM is adopted in coupling to the dynamic mooring line model. Details of the solver are referred to Zhong et al. (2020a, 2020b). The PIMPLE algorithm is used to treat the pressure-velocity coupling problem. The principal of the algorithm is as follows: within each time step, both the inner pressure correction loop (PISO loop) and outer pressure-momentum correction loop (SIMPLE loop) are executed. In the inner loop, the pressure is recalculated with

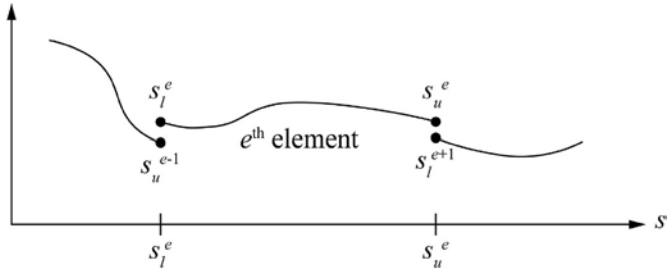

Fig. 1. Discontinuity across segments in the LDG FEM dynamic mooring line model.

Fig. 2. Demonstration of the DeepCwind semi-submersible platform (Robertson et al., 2017).

Table 1
Main parameters of the DeepCwind semi-submersible platform.

Parameter	Value
Depth of platform base below SWL	20 m
Elevation of central column above SWL	10 m
Displacement	13986.8 m^3
Mass (including ballast)	1.3473×10^7 kg
Center of mass location below SWL	14.40 m
Platform roll inertia about CM	8.011×10^9 kg m^2
Platform pitch inertia about CM	8.011×10^9 kg m^2
Platform yaw inertia about centerline	1.391×10^{10} kg m^2

Table 2
Main parameters of the mooring system for the DeepCwind semi-submersible platform.

Parameter	Value
Unstretched length	835.5 m
Diameter	0.0766 m
Equivalent mass density	113.35 kg/m
Equivalent axial stiffness	7.536×10^8 N
Normal drag coefficient	2.00
Tangential drag coefficient	0.40
Normal Added mass coefficient	0.80
Tangential added mass coefficient	0.25

the new updated flux. In the outer loop, the velocity matrix is first rebuilt with the new flux, the pressure is then corrected with the new velocity matrix and the flux is finally corrected with the new pressure. The calculations are repeated until convergence is achieved. The solutions are regarded as being converged when the residuals of the velocity and pressure are lower than 1E-06.

2.2. Rigid body dynamics

The floating platform is treated as rigid body moving with six DOFs, i.e., surge, sway, heave, roll, pitch and yaw. The listed DOFs follow the order of linear and rotational motions along or around x, y and z axes. The structural motion is computed via the rigid body solver in OpenFOAM that uses an explicit time step marching within PIMPLE loop. The forces and moments are obtained by integrating pressure and viscous stress over the structural surface as

$$\boldsymbol{F} = \iint_S (p\boldsymbol{n} + \boldsymbol{\tau}) dS + \boldsymbol{F}_M \tag{7}$$

$$\boldsymbol{M} = \iint_S (\boldsymbol{r}_{CS} \times (p\boldsymbol{n} + \boldsymbol{\tau})) dS + \boldsymbol{r}_{CM} \times \boldsymbol{F}_M \tag{8}$$

where $\boldsymbol{F_M}$ is the restoring force from the dynamic mooring line model. $\boldsymbol{r}_{CM}$ and $\boldsymbol{r}_{CS}$ denote the distance vector of the structural mass center to the mooring attachment point and the cell surface center, respectively.

In the motion solver, the fluid forces and moments calculated with equations (7) and (8) together with the gravity force are exerted onto the structure to obtain the linear and angular accelerations with Newton's second law. Velocities and displacements of the platform are calculated with the Newmark method (Belytschko et al., 2014) as

$$\dot{\boldsymbol{d}}_{i+1} = \dot{\boldsymbol{d}}_i + \Delta t \left[(1-\gamma)\ddot{\boldsymbol{d}}_i + \gamma \ddot{\boldsymbol{d}}_{i+1} \right] \tag{9}$$

$$\boldsymbol{d}_{i+1} = \boldsymbol{d}_i + \Delta t \dot{\boldsymbol{d}}_i + \Delta t^2 \left[(0.5-\beta)\ddot{\boldsymbol{d}}_i + \beta \ddot{\boldsymbol{d}}_{i+1} \right] \tag{10}$$

where the symbol $\boldsymbol{d}$ denotes the displacement vector, and single and double dots over $\boldsymbol{d}$ mean its first and second derivatives respectively. β and γ are numerical parameters specified to 0.25 and 0.5 respectively representing the implicit and unconditionally stable scheme.

2.3. Mesh deformation

To accommodate the moving platform in the numerical domain, the mesh adjusts with the structural motion. The adjustment realizes through grid deformation governed by the Laplace equation below.

$$\nabla \cdot (\gamma_M \nabla \boldsymbol{d}_M) = 0 \tag{11}$$

where γ_M is the variable diffusivity based on the inverse square of the distance between cell centers and moving boundaries as

$$\gamma_M = \frac{1}{r_M{}^2} \tag{12}$$

3. Coupled CFD and dynamic mooring line model

3.1. Mooring dynamics

The mooring dynamics represented with the LDG FEM is used (Palm et al., 2017). The dynamics of flexible mooring lines is governed by a vector-valued wave equation formulated in the global inertia frame as

$$\frac{\partial^2 \boldsymbol{r}}{\partial t^2} = \frac{1}{\gamma_0}\frac{\partial \boldsymbol{T}}{\partial s} + \frac{\boldsymbol{f}}{\gamma_0} \tag{13}$$

where γ_0 is the mooring line mass per meter. $\boldsymbol{r}$ denotes the cable position in the inertia frame and s is the curvilinear abscissa along the unstretched line. In the mooring dynamics, only the extensional stiffness is included while the bending and torsional stiffnesses are ignored. Thus, the internal moment $\boldsymbol{M}$ is simply set to zero in the modeling, and the axial tension force vector $\boldsymbol{T}$ is always tangential to the cable as

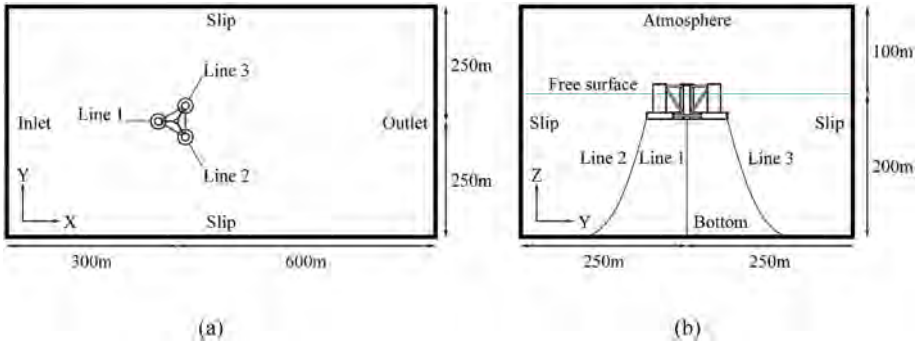

Fig. 3. Computational domain of the free-decay and dynamic responses under regular waves of the DeepCwind semi-submersible platform: (a) View from top; (b) View from outlet.

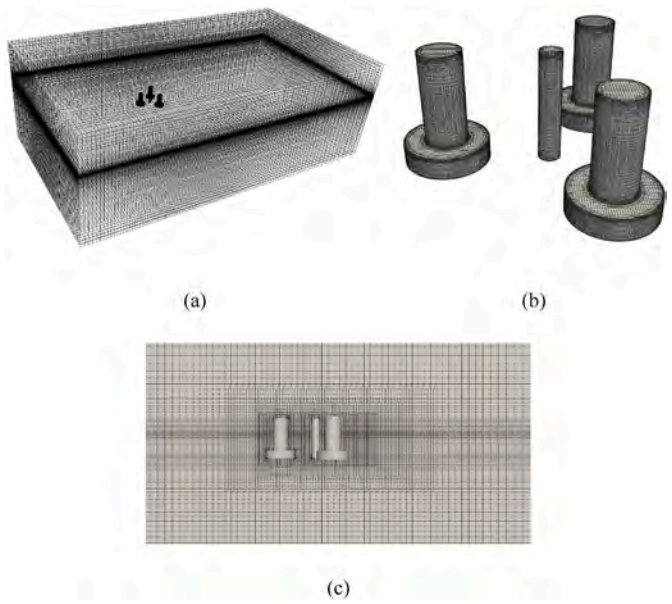

Fig. 4. Mesh arrangement for the free-decay and dynamic responses under regular waves of the DeepCwind semi-submersible platform: (a) Global view; (b) Local view; (c) Cutaway view.

$$\boldsymbol{T} = T(\varepsilon, \dot{\varepsilon})\frac{\boldsymbol{q}}{1+\varepsilon} \tag{14}$$

$$\boldsymbol{q} = \frac{\partial \boldsymbol{r}}{\partial s} \tag{15}$$

$$\varepsilon = |\boldsymbol{q}| - 1 \tag{16}$$

where ε is the axial strain. T is the magnitude of tension which contains the constitutive relation of the mooring line as a function of strain and strain rate. For a linear elastic cable, the tension force expresses as

$$T(\varepsilon) = EA\varepsilon \tag{17}$$

The symbol $\boldsymbol{f}$ in equation (13) represents all external forces on the mooring line (Palm et al., 2017) as

$$\boldsymbol{f} = \boldsymbol{f}_a + \boldsymbol{f}_b + \boldsymbol{f}_c + \boldsymbol{f}_d \tag{18}$$

$\boldsymbol{f_a}$ includes the inertia force and the added mass force which exist for structures accelerating in fluids as

$$\boldsymbol{f}_a = \rho_f A_0\left(C_{at}\boldsymbol{a}_{r,t} + C_{an}\boldsymbol{a}_{r,n} + \boldsymbol{a}_f\right) \tag{19}$$

where C_a is the added mass coefficient, and subscripts t and n mean the tangential and normal directions respectively. $\boldsymbol{a}$ is the acceleration vector. A_0 is the cross-sectional area of unstretched cable line.

$\boldsymbol{f_b}$ is the net force from buoyancy written as

$$\boldsymbol{f}_b = \gamma_0\frac{\rho_c - \rho_f}{\rho_c}\boldsymbol{g} \tag{20}$$

where ρ_c and ρ_f are the material density of the mooring line and fluid, respectively.

$\boldsymbol{f_c}$ is the contact force between the mooring line and the seabed. The bilinear spring and damper model is used for the normal force to the contact plane, and the dynamic friction is implemented for the tangential force. For a horizontal sea floor, the contact force vector is given as

$$\boldsymbol{f}_c = \begin{cases} \boldsymbol{G}_v + \boldsymbol{G}_h \ if(z_G - r_z) \geq 0 \\ 0 \ otherwise \end{cases} \tag{21}$$

$$\boldsymbol{G}_v = \left(K_G d_c(z_G - r_z) - 2\xi_G\sqrt{K_G\gamma_0 d_c}\max(\dot{r}_z, 0)\right)\boldsymbol{z} \tag{22}$$

$$\boldsymbol{G}_h = \mu_c f_{b_z}\tanh\left(\frac{\pi\dot{r}_{xy}}{v_\mu}\right)\frac{\dot{\boldsymbol{r}}_{\boldsymbol{xy}}}{|\dot{\boldsymbol{r}}_{xy}|} \tag{23}$$

where z_G is the vertical position of the seabed. K_G and ξ_G are the stiffness and ratio of critical damping for the cable-seabed interaction, respectively. μ_c is the friction coefficient with a user-specified velocity v_μ for the maximum friction.

$\boldsymbol{f_d}$ is the drag force proportional to the square of the relative velocity between the structure and fluid as

$$\boldsymbol{f}_d = \rho_f d\sqrt{1+\varepsilon}\left(C_{Dt}|\boldsymbol{v}_{r,t}|\boldsymbol{v}_{r,t} + C_{Dn}|\boldsymbol{v}_{r,n}|\boldsymbol{v}_{r,t}\right)\Big/ 2 \tag{24}$$

where C_D is the drag coefficient, and $\boldsymbol{v}$ is the velocity vector.

The LDG FEM with Legendre basis functions φ_k of arbitrary order p is used to spatially discretize the dynamic equation of mooring line. The discontinuity between elements of the method emerges when deriving the weak form of the governing equation with the numerical flux represented by terms with overbar on the right-hand side of equations (25) and (26). These equations are manipulated on the eth element with the boundaries denoted by s_l^e and s_u^e as shown in Fig. 1. Note that equations (25) and (26) correspond respectively to the non-dimensional version of equations (13) and (15) by scaling $\boldsymbol{r}$ and s with a characteristic length L_c and by scaling the time with a characteristic time t_c. c denotes the nonlinear and non-dimensional celerity of the wave propagation and is defined in equation (27).

$$\int_{\Omega^e}\varphi_k\frac{\partial^2\boldsymbol{r}_h}{\partial t^2}d\Omega = \left(\varphi_k\overline{c_h{}^2\boldsymbol{q}_h}^e\right)\Big|_{s_l^e}^{s_u^e} - \int_{\Omega^e}\frac{\partial\varphi_k}{\partial s}c_h{}^2\boldsymbol{q}_h d\Omega + \int_{\Omega^e}\varphi_k\boldsymbol{f}_h d\Omega \tag{25}$$

$$\int_{\Omega^e}\varphi_k\boldsymbol{q}_h d\Omega = \left(\varphi_k\overline{\boldsymbol{r}}_h^e\right)\Big|_{s_l^e}^{s_u^e} - \int_{\Omega^e}\frac{\partial\varphi_k}{\partial s}\boldsymbol{r}_h d\Omega \tag{26}$$

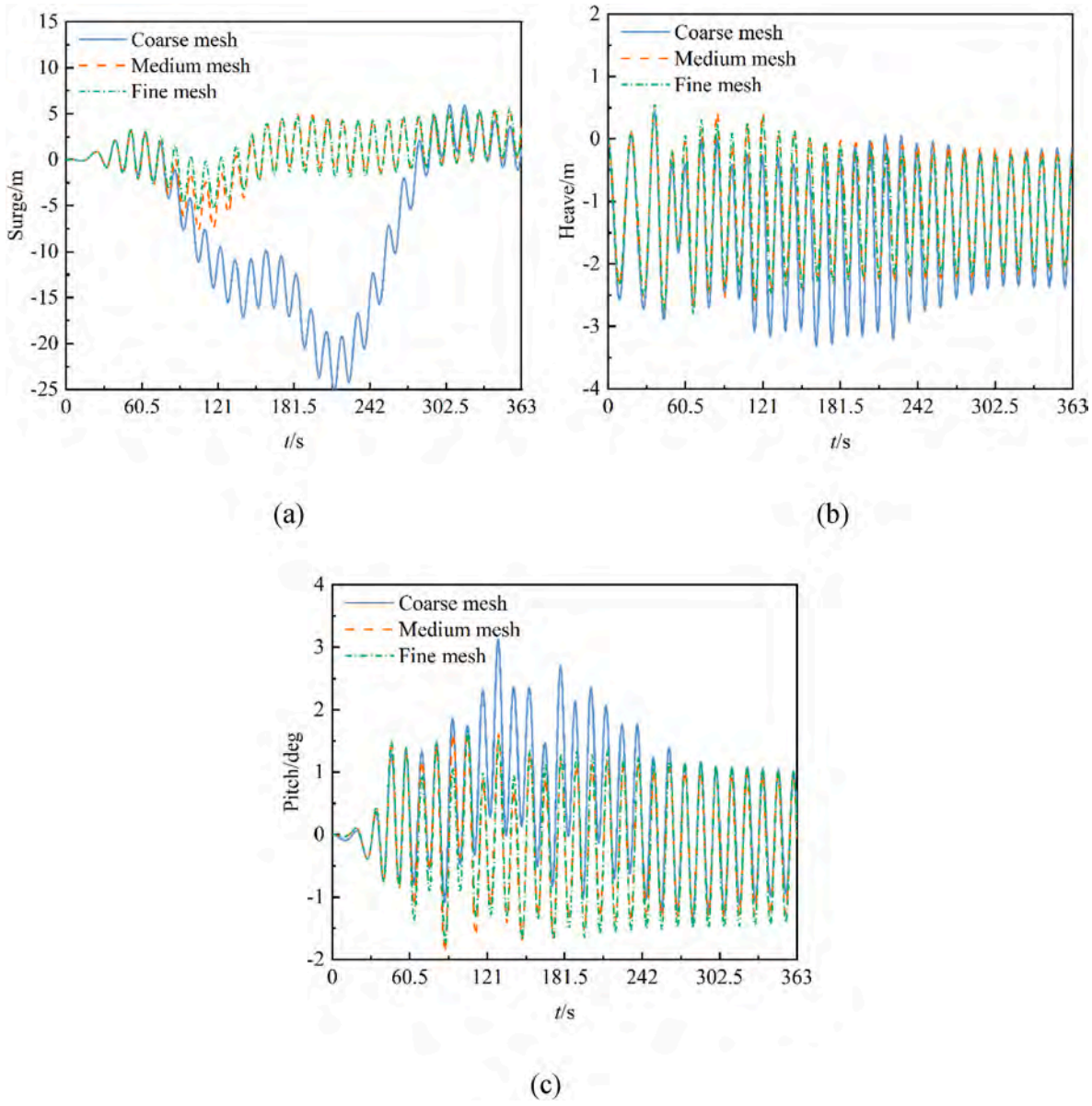

Fig. 5. Mesh convergence study for the dynamic responses of the DeepCwind semi-submersible platform under regular wave with a height of 10.30 m and a period of 12.1s: (a) Surge motion; (b) Heave motion; (c) Pitch motion.

$$c^2 = \frac{t_c^2}{L_c^2}\frac{EA_0}{\gamma_0}\frac{\varepsilon}{1+\varepsilon} \tag{27}$$

To utilize the finite volume possibility via the numerical flux term in LDG, the approach in Cockburn and Shu (1998) is used as given by

$$\overline{\boldsymbol{r}_h} = \{\boldsymbol{r}_h\} - \beta[\boldsymbol{r}_h] \tag{28}$$

$$\overline{c_h^2\boldsymbol{q}_h} = \{c_h^2\boldsymbol{q}_h\} - \beta[c_h^2\boldsymbol{q}_h] + \eta_1[\boldsymbol{r}_h] \tag{29}$$

where β defined in $[-1, 1]$ controls from which direction to weight the numerical flux. η_1 is a case dependent penalty parameter. The trace $\{x\}$ and jump $[x]$ operators are given by

$$\{x_h^e\}|_s = \frac{1}{2}\left(x_h^e|_{s_u^e} + x_h^{e+1}|_{s_l^{e+1}}\right) \text{ if } s = s_u^e \tag{30}$$

$$\{x_h^e\}|_s = \frac{1}{2}\left(x_h^e|_{s_l^e} + x_h^{e-1}|_{s_u^{e-1}}\right) \text{ if } s = s_l^e \tag{31}$$

$$[x_h^e]|_s = \frac{1}{2}\left(x_h^e|_{s_u^e} - x_h^{e+1}|_{s_l^{e+1}}\right) \text{ if } s = s_u^e \tag{32}$$

$$\{x_h^e\}|_s = \frac{1}{2}\left(x_h^{e-1}|_{s_u^{e-1}} - x_h^e|_{s_l^e}\right) \text{ if } s = s_l^e \tag{33}$$

One prominent feature of the high order method is the exponential convergence in smooth solutions, e.g., hanging catenary, and thus sufficient accuracy can be obtained in engineering applications using only a few high order elements. The dynamic equation advances in time with the second order explicit Leap-Frog scheme. The time step size in the mooring model is restricted by the mesh size and order to maintain numerical stability. Due to the high stiffness in the mooring line, the time step size in the mooring solver is in general much smaller than that of the CFD solver.

3.2. Coupling of CFD and mooring line model

During the coupled simulation, the mooring attachment points on

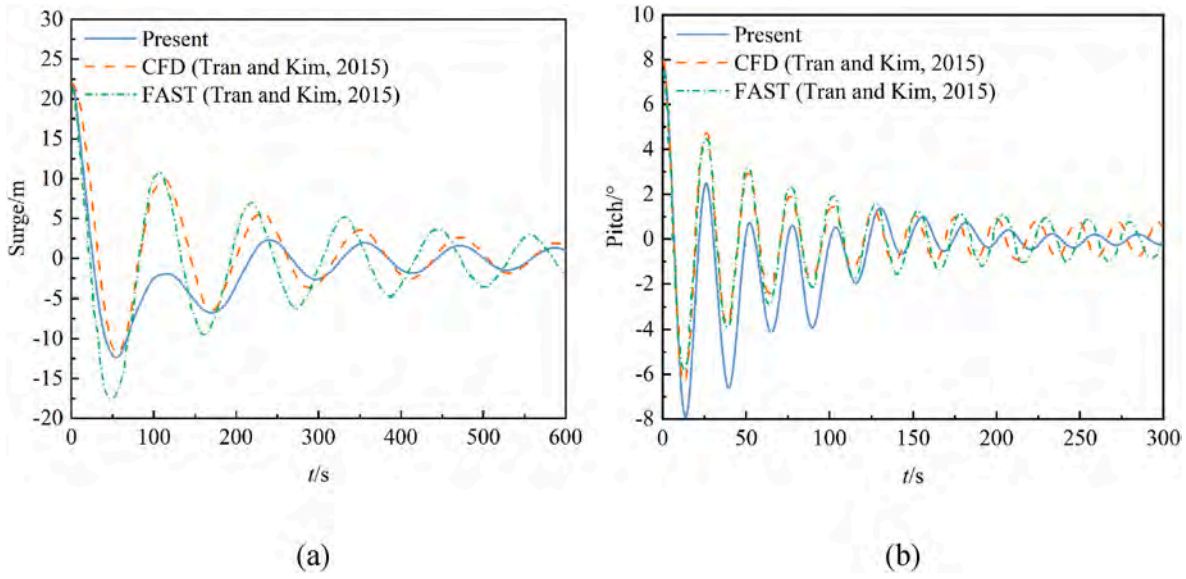

Fig. 6. Free-decay motion responses of the DeepCwind semi-submersible platform: (a) Surge DOF; (b) Pitch DOF.

Table 3
Comparison of free-decay motion natural periods of the DeepCwind semi-submersible platform.

Method	Surge	Sway	Heave	Roll	Pitch	Yaw
Present	118.5 s (+10.7%)	111.6 s (−0.4%)	17.6 s (+0.6%)	25.9 s (−3.7%)	25.8 s (−3.7%)	94.1 s (+14.3%)
Experiment (Coulling et al., 2013)	107.0 s	112.0 s	17.5 s	26.9 s	26.8 s	82.3 s
FAST (Coulling et al., 2013)	107.0 s (0.0%)	113.0 s (+0.9%)	17.3 s (−1.1%)	26.7 s (−0.7%)	26.8 s (0.0%)	82.7 s (+0.5%)
Simo/Riflex + TDHMILL (Luan et al., 2013)	115.9 s (+8.3%)	110.8 s (−1.1%)	17.1 s (−2.3%)	26.0 s (−3.3%)	25.8 s (−3.7%)	80.2 s (−2.6%)
AQWA (Tran and Kim, 2015)	112.5 s (+5.1%)	112.5 s (+0.4%)	17.3 s (−1.1%)	25.4 s (−5.6%)	25.4 s (−5.2%)	83.7 s (+1.7%)
CFD (Tran and Kim, 2015)	108.1 s (+1.0%)	114.5 s (+2.2%)	17.8 s (+1.7%)	25.3 s (−5.9%)	25.2 s (−6.0%)	83.3 s (+1.2%)

Table 4
Parameters of the regular waves.

Cases	Amplitude	Period
1	3.79 m	12.1 s
2	3.57 m	14.3 s
3	3.79 m	20.0 s
4	5.15 m	12.1 s
5	5.37 m	14.3 s
6	5.56 m	20.0 s

the platform are used as Dirichlet boundary conditions for the mooring solver. Then the resultant force from each mooring line is returned to the CFD solver for the rigid body dynamics. The force and moment are represented by the last term in equations (7) and (8), respectively. Since difference in time step length exists between the coupled solvers, interpolation in time is required for imposing the boundary conditions. In the coupling, the mooring solver is lagging a fraction φ of the latest time step in the CFD solver as (e.g., at the kth time step)

$$t_m^k = (1-\varphi)t_f^k + \varphi t_f^{k-1} \tag{34}$$

where t_f^k and t_m^k denote the kth time in the fluid and mooring solvers, respectively.

The mooring line boundary conditions at the fairlead are interpolated using the latest mooring attachment point position P_k based on constant acceleration as

$$r_k(\tau) = r(0) + (v(0) + 0.5a_k\tau)\tau \tag{35}$$

$$v_k(\tau) = v(0) + a_k\tau \tag{36}$$

$$a_k = \frac{1}{0.5\Delta t_k{}^2}(P_k - r_k(0) - v_k(0)\Delta t_k) \tag{37}$$

where τ in [0, t_m^k-t_m^{k-1}] is the local time in the interpolation interval, and Δt_k is the time interval of constant acceleration.

4. Freak wave generation and absorption

4.1. Freak wave modeling

The freak wave is modeled with the NewWave theory which describes the surface elevation and wave velocity of a focused group of localized waves derived from a selected spectrum (Ning et al., 2009). The wave components are brought into phase at specified time and location, thus generating extreme wave events in an expected way. The JONSWAP spectrum is employed in the present study (Hasselmann et al., 1973). The significant wave height H_s, peak frequency ω_p and shape factor γ are the main parameters to the spectrum as

$$S(\omega) = \frac{5}{16}H_s{}^2\omega_p{}^4\omega^{-5}\ EXP\Bigg\{ -\frac{5}{4}(\omega/\omega_p)^{-4}\Bigg\}(1-0.287\ Ln(\gamma))\gamma^{EXP\left\{-\frac{1}{2}\left(\frac{\omega-\omega p}{\sigma\omega p}\right)^2\right\}} \tag{38}$$

$$\sigma = \begin{cases} 0.07\ \omega \le \omega p \\ 0.09\ \omega > \omega p \end{cases} \tag{39}$$

With the spectrum in hand, the amplitude of each wave component is determined with the following equation.

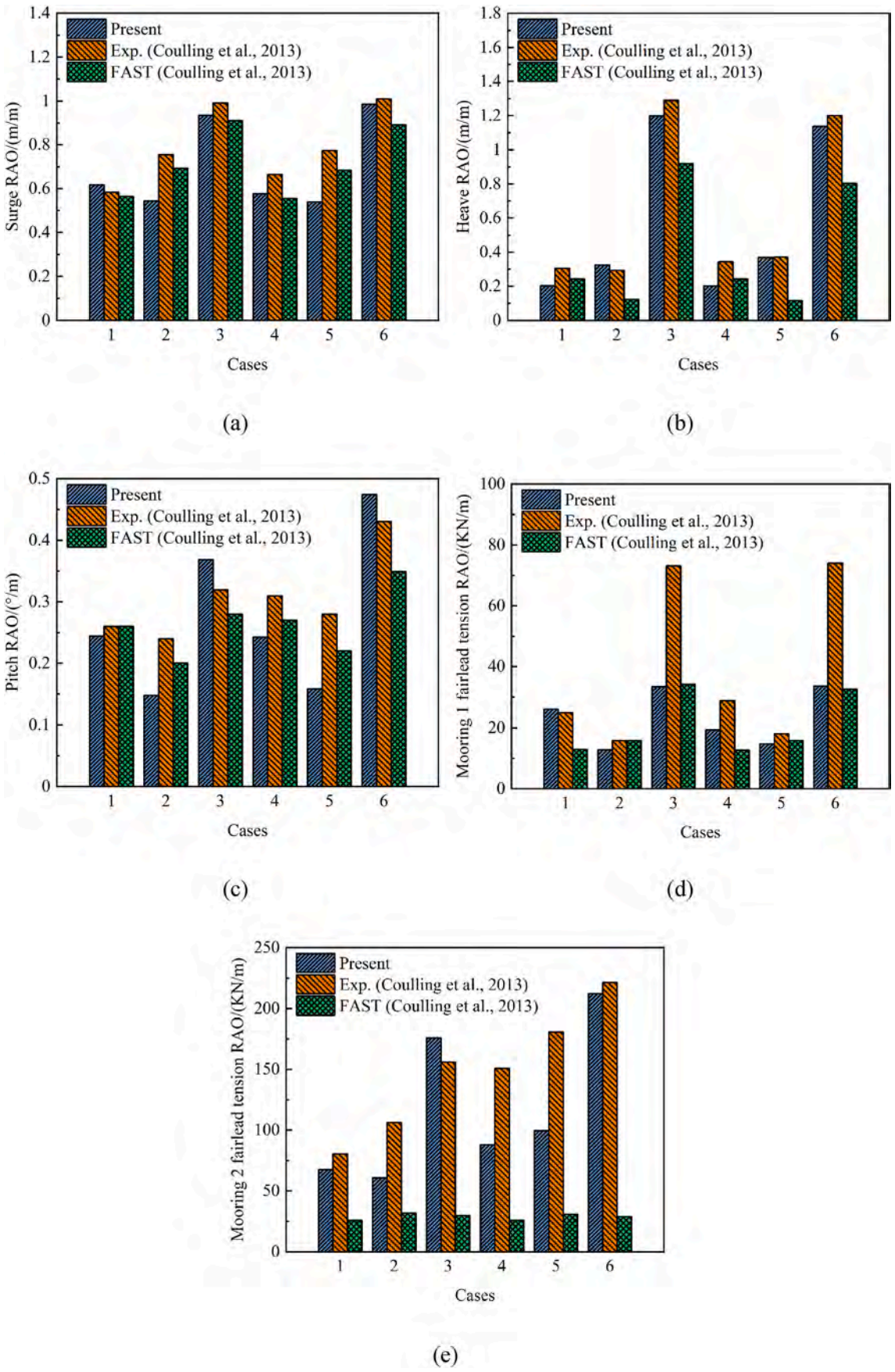

Fig. 7. RAOs of the DeepCwind semi-submersible platform under regular waves: (a) Surge RAO; (b) Heave RAO; (c) Pitch RAO; (d) Mooring line 1 fairlead tension RAO; (e) Mooring line 2 fairlead tension RAO.

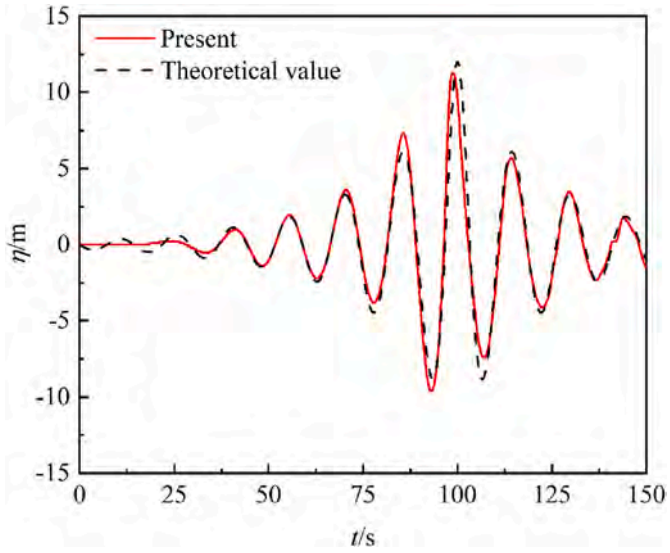

Fig. 8. Comparison of the free surface elevation time history at location x = 300 m of the freak wave with a focusing time of 100s and location of 300 m.

$$A_i = A_{\max}\frac{S_i(\omega)\Delta\omega}{\sum_{i=1}^{n} S_i(\omega)\Delta\omega} \tag{40}$$

where $\Delta\omega$ is the frequency step depending on the bandwidth and wave component number n. $A_{\max}$ is the targeted crest amplitude of the freak wave.

The input wave signal for the CFD runs can be first order only or sum of first and second orders. For details see Westphalen et al. (2012). For the study here, only first order wave theory is utilized. Formula for the free surface elevation and wave velocity components are given as

$$\eta_i = A_i \cos(k_i x - \omega_i t + \varepsilon_i) \tag{41}$$

$$u_i = \frac{A_i k_i g}{\omega_i}\frac{\cosh k_i(z+h)}{\cosh k_i h}\cos(k_i x - \omega_i t + \varepsilon_i) \tag{42}$$

$$w_i = \frac{A_i k_i g}{\omega_i}\frac{\sinh k_i(z+h)}{\cosh k_i h}\sin(k_i x - \omega_i t + \varepsilon_i) \tag{43}$$

Where ε_i is the phase shift for each wave component and is obtained according to the focusing time $t_{\max}$ and location $x_{\max}$ as

$$\varepsilon_i = \omega_i t_{\max} - k_i x_{\max} \tag{44}$$

Thus, the input data at the inlet boundary is calculated as

$$\eta = \sum_{i=1}^{n} A_i \cos[\omega_i(t_{\max} - t) - k_i x_{\max}] \tag{45}$$

$$u = \sum_{i=1}^{n} \frac{A_i k_i g}{\omega_i}\frac{\cosh k_i(z+h)}{\cosh k_i h}\cos[\omega_i(t_{\max} - t) - k_i x_{\max}] \tag{46}$$

$$w = \sum_{i=1}^{n} \frac{A_i k_i g}{\omega_i}\frac{\sinh k_i(z+h)}{\cosh k_i h}\sin[\omega_i(t_{\max} - t) - k_i x_{\max}] \tag{47}$$

4.2. Active wave absorption

Reflected waves at the wavemaker side and propagating waves at the outlet are actively absorbed following the strategy in Higuera et al. (2013). The activeness is in the sense that the wavemaker or the absorbing boundary adjusts based on real time measurements for target wave. The wave absorption is based on the shallow water theory which describes the velocity along the water column height as constant. This is viable as experiences with other numerical models have shown that it works relatively well for waves outside the shallow water range. Thus, the following equation is derived.

$$Uh = c\eta \tag{48}$$

where U is the vertically integrated horizontal velocity. c is the wave celerity which can be approximated by

$$c = \sqrt{gh}\,\frac{a_0 + a_1(kh)^2}{1 + b_1(kh)^2} \tag{48}$$

where the coefficients a_0, a_1 and b_1 are respectively set to 1, 0 and 0 for the present absorption theory in consideration of shallow water assumption although improvements could be obtained with digital filter coefficients.

The correction velocity U_c which opposes the incoming one can then be arranged as

$$U_c = -\sqrt{\frac{g}{h}}\eta_r \tag{49}$$

where η_r is obtained by subtracting the measured free surface elevation from the target one for free of reflection.

For true 3D wave absorption considered in the present study, correction velocity can only be applied on the direction perpendicular to the boundary rather than formulating a quasi-3D absorption as the nearby wave directionality is distorted due to continuously velocity correction. In this case, the velocity component perpendicular to the boundary is resolved from equation (49). The tangential component of the velocity is left unmodified so that it can be measured. For occasions when the tangential velocity is greater than the total velocity modulus, a correction value of zero is used as no absorption takes place.

5. Model validations

5.1. Coupled CFD-mooring model

To demonstrate the validity of the coupled CFD-mooring model, free-decay and dynamic responses under regular waves of the DeepCwind platform moored by three catenary lines are simulated (Robertson et al., 2017). The semi-submersible structure has been extensively studied in the FOWT community, e.g., Coulling et al. (2013), Liu et al. (2017) and Tran and Kim (2015). The platform consists of three offset columns with larger diameter base columns functioned as heave plates, one central column connecting to the tower base, four sets of level pontoons and three cross braces as shown in Fig. 2. The three mooring lines are evenly distributed around the platform with the fairleads attached at the top of base columns, i.e., 40.868 m from the centerline and 14 m below the still water level (SWL), and the anchors 837.6 m away from the centerline at a water depth of 200 m. Gross properties of the platform and mooring systems are shown in Table 1 and Table 2, respectively. For details see Robertson et al. (2017). The mass property of the structure has been adjusted in the present numerical study to account for the mounted wind turbine and is kept in line with the 1:50 scale model test by Coulling et al. (2013). A full-scale DeepCwind platform is modeled in the simulations as was used in Huang et al. (2019) and Tran and Kim (2015). The computational layout with a total dimension of 900m × 500m × 300 m is shown in Fig. 3. For the mesh convergence, the platform response under regular wave with a height of 10.30 m and a period of 12.1s is simulated, and three grids with total cells of 1,269,560, 1,998,118 and 3,461,799 are compared. Fig. 4 shows the views of the generated mesh with medium density. Note that to reduce the computational costs, the pontoons and cross braces are not included in the modeling (Huang et al., 2021). The convergence results are visualized in Fig. 5. It is seen that the medium mesh which has a minimum cell side length of 0.5 m near the free surface and the structure can be a proper choice for the

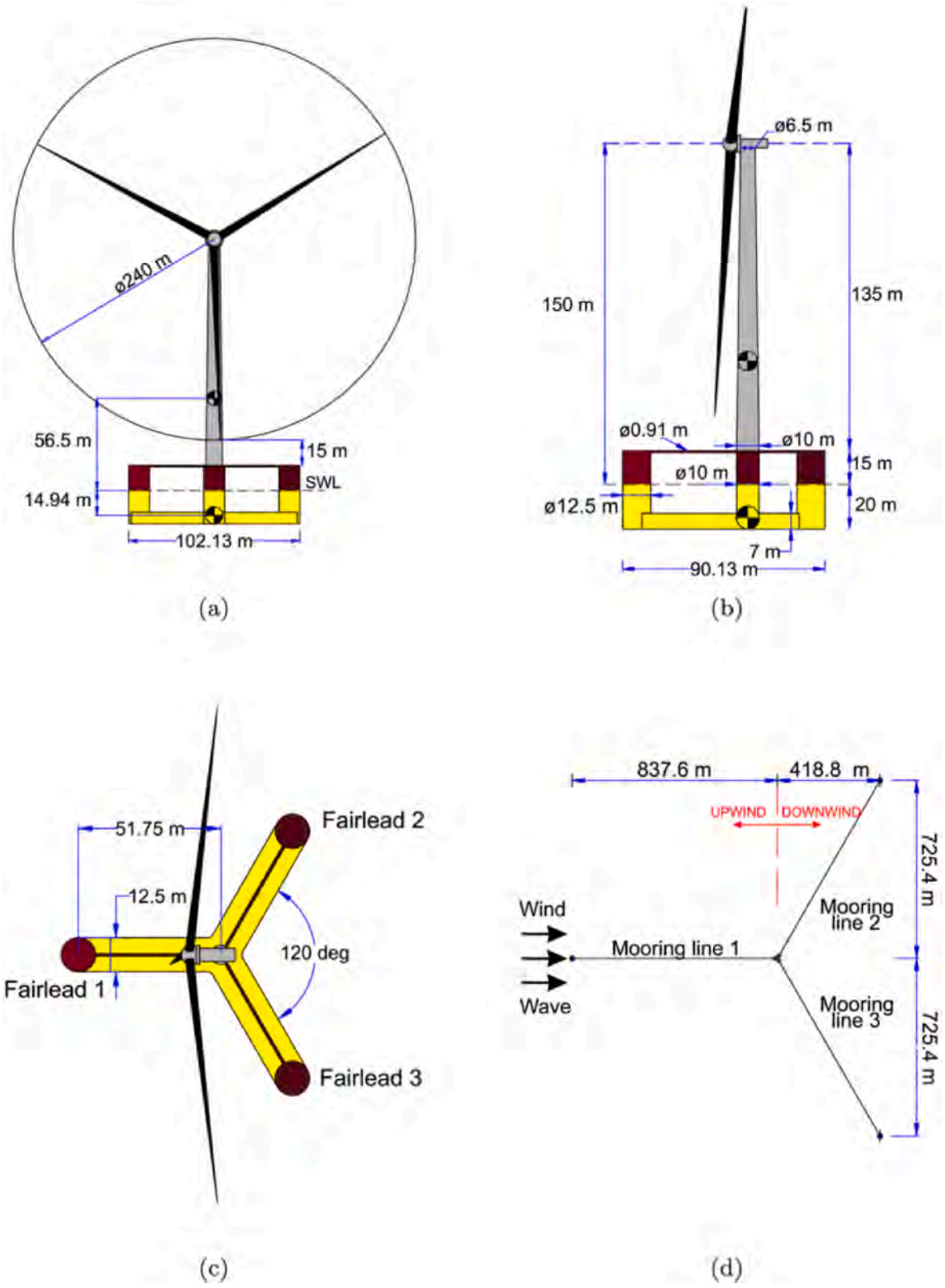

Fig. 9. Schematic of the IEA 15 MW wind turbine mounted on the VolturnUS-S semi-submersible platform: (a) Front view; (b) Side view; (c) Top view; (d) Plan view of the mooring system.

present simulations. The calculated y^+ values over the platform hull are between 150.0 and 200.0 which stay in the range of the inertial sublayer.

The free-decay motions in six DOFs are considered. In the test, the platform is released from an initial position away from the equilibrium state. The initial offsets for surge, sway, heave, roll, pitch and yaw DOFs are 22 m, 20 m, 4 m, 15°, 8° and 10°, respectively (Tran and Kim, 2015). The free-decay motion responses of the platform in surge and pitch are

Table 5
Main parameters of the VolturnUS-S semi-submersible platform.

Parameter	Value
Depth of platform base below SWL	20 m
Elevation of central column above SWL	15 m
Displacement	20206.0 m^3
Mass (including ballast)	1.7854×10^7 kg
Center of mass location below SWL	14.94 m
Platform roll inertia about CM	1.251×10^{10} kg m^2
Platform pitch inertia about CM	1.251×10^{10} kg m^2
Platform yaw inertia about centerline	2.367×10^{10} kg m^2

shown in Fig. 6. The predicted results are compared with existing numerical results obtained by the potential flow model-based and CFD methods. As shown in Fig. 6, the present results show generally similar variation trend with the published data, but there exist some discrepancies in the time history responses especially in surge DOF. The reason for this may be the introduction of mooring dynamics in the simulations while either spring or quasi-static mooring model was used in Tran and Kim (2015). It is also observed that the CFD simulations predict the lowest magnitude of surge response during each free-decay circle, which is regarded as the effect of the inclusion of fluid viscosity compared to the potential flow model-based approach. The calculated periods of the free-decay motions are compared to the experimental and numerical results in Table 3. Relative errors with respect to the experimental data are shown in parentheses. It is seen that the results obtained by the present CFD-mooring model exhibit a good agreement to the MARIN test data (Coulling et al., 2013). The perfect match of FAST results to the experiments is due to the tuned drag and added mass coefficients used in the hydrodynamic module HydroDyn which adopts the potential flow theory (Coulling et al., 2013). Except for the FAST results, the present model gives lower error in motion period than other numerical results (Luan et al., 2013; Tran and Kim, 2015). It is noted that a simplified semi-submersible platform with no pontoons and cross braces is used in the present simulations, which contributes to the deviations in results. Furthermore, considering the scale effect, structural flexibility of the platform, and uncertainties in the experiments, the errors in free-decay period for the present model are acceptable.

The dynamic responses of the moored semi-submersible platform under regular waves are simulated with the coupled CFD-mooring model. Parameters of the waves are given in Table 4. The response amplitude operator (RAO) defined as the response amplitude of a field variable per amplitude of the regular wave is used to evaluate the platform hydrodynamics. The motion responses in surge, heave and pitch are analyzed herein due to the symmetry of the flow field around the platform as indicated by Fig. 3.

The RAOs of motions and mooring line fairlead tensions are plotted in Fig. 7, in which the experimental data and FAST results from Coulling et al. (2013) are used for comparison. The x-axis label in the figure is related to the case order in Table 4. It is seen that the RAOs obtained by the CFD-mooring model show better agreement with the experiments than FAST. The large discrepancy for FAST computation is likely due to its quadratic damping model which depends on empirical coefficients

Table 6
Main parameters of the mooring system for the VolturnUS-S semi-submersible platform.

Parameter	Value
Unstretched length	850.0 m
Volume-equivalent diameter	0.3330 m
Equivalent mass density	685.00 kg/m
Equivalent axial stiffness	3.270×10^9 N
Normal drag coefficient	1.11
Tangential drag coefficient	0.20
Normal Added mass coefficient	0.82
Tangential added mass coefficient	0.27

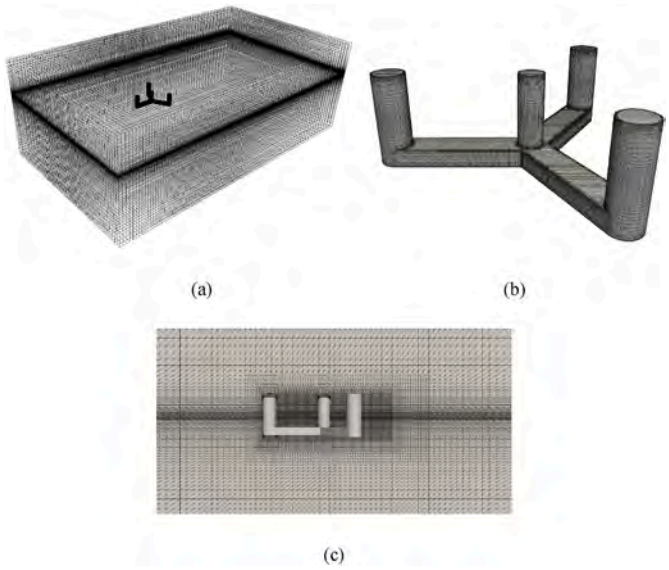

Fig. 10. Mesh arrangement for the dynamic responses under freak waves of the VolturnUS-S semi-submersible platform: (a) Global view; (b) Local view; (c) Cutaway view.

for estimating hydrodynamic loads. It is shown in Fig. 7 that the platform motions when the wave period equals 20.0s are evidently larger than those at the values of 12.1s and 14.3s. It means that the hydrodynamics of the platform is more sensitive to low-frequency waves than high-frequency waves. This is consistent with the OC5 project phase II group which states that the ultimate and fatigue loads of the floating platform under wave impacts are severely underpredicted in the low-frequency region (Robertson et al., 2017). Fig. 7 also shows that the RAOs rise with the wave amplitude at the same wave period which is in contrast to the linear theory. It implies the nonlinearity in the response of the platform associated with the fluid viscosity which is ignored in the potential flow model.

5.2. Freak wave generation

The freak wave modeling is realized utilizing the OpenFOAM irregular wave generation library with the wave properties imposed at the inlet as Dirichlet condition (Wang et al., 2019). The focusing time and location are predefined and then manually embedded into each wave component description according to the wave spectrum and frequency range and step before setting up the input dictionary. The wave considered for the validation has a focusing time of 100s and location of 300 m. The computational domain is a 2D version of that used for the coupled CFD-mooring model validation shown in Fig. 3 with the platform removed. The settings guarantee that as least 10 cycles of the wave component with the smallest length pass the focusing point before the focusing phenomenon occurs. The simulated free surface elevation time history recorded at the location $x = 300$ m as well as the theoretical value is shown in Fig. 8. It is observed that the present results agree generally well with the theoretical ones. It is noted that the small

Table 7
Parameter range for the hydrodynamic study on the VolturnUS-S semi-submersible platform under freak waves.

Parameter	Value
Focusing crest amplitude	8 m, 10 m, 12 m
Focusing location relative to the platform center	−51.75 m, −34.50 m, −17.25 m, 0.00 m, 17.25 m, 34.50 m, 51.75 m
Wave incident angle	0°, 15°, 30°, 45°, 60°
COG of the platform	(-0.2 m, −2.2 m), (0.0 m, −1.0 m), (0.0 m, −2.2 m), (0.0 m, −3.5 m)

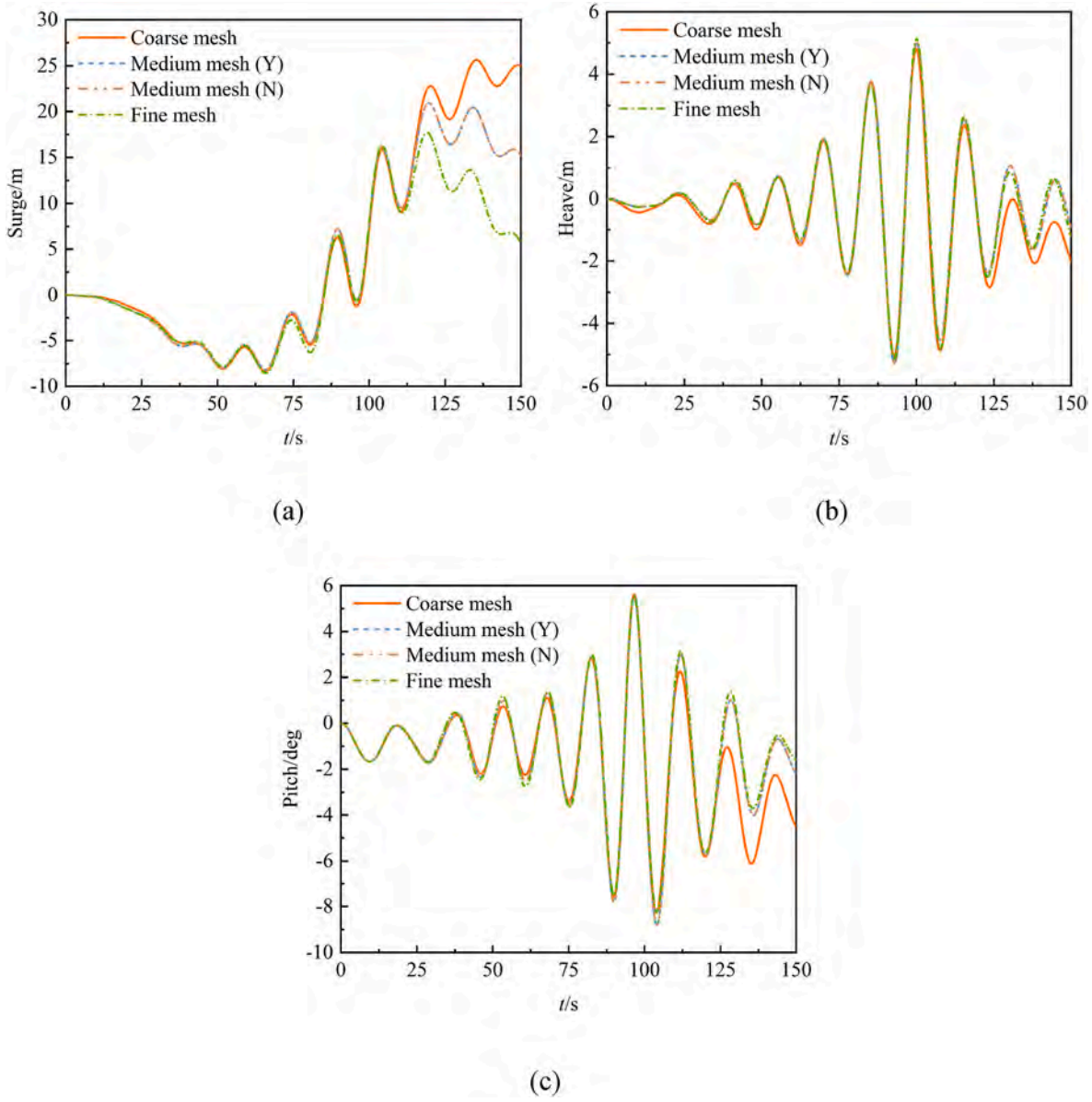

Fig. 11. Mesh convergence study for the dynamic responses of the VolturnUS-S semi-submersible platform under freak wave with a focusing crest amplitude of 12 m: (a) Surge motion; (b) Heave motion; (c) Pitch motion.

discrepancies at the times around focusing may be due to the numerical errors associated with CFD and are regarded as acceptable for the present investigation purpose.

6. Computational details

6.1. Physical model

The present study aims to investigate the hydrodynamics of the UMaine VolturnUS-S semi-submersible platform under the impact of freak waves (Allen et al., 2020). This floater structure is designed for supporting the IEA 15 MW wind turbine which indicates the trend of large-scale wind turbines (Gaertner et al., 2020). As shown in Fig. 9, the reference platform consists of one main column on which the wind turbine tower is mounted, three offset columns radially placed surrounding the central tower, and three rectangular bottom pontoons connecting offset columns to the central one. The whole FOWT is deployed in a water depth of 200 m and the draft of the platform is 20 m under SWL. A ballast system including an iron-ore-concrete ballast fixed at the bottom of the offset columns and seawater ballast contained in the pontoons and the central column is used to maintain the designed draft. Three catenary mooring lines equally arranged around the semi-submersible platform is used for keeping the structure in place (See Fig. 9(d)). Parameters of the complete system are depicted in Fig. 9 and the gross properties are presented in Table 5 and Table 6.

6.2. Numerical setup

The numerical setup for the UMaine VolturnUS-S semi-submersible platform is the same as that for the DeepCwind platform shown in Fig. 3. The computational domain is sized to 900 m, 500 m and 300 m in the x, y and z coordinates, respectively. The freak wave propagates from the leftmost boundary to the outlet at the rightmost boundary as indicated by Fig. 3, and the platform locates 300 m downstream of the wavemaker. A medium density mesh is generated as plotted in Fig. 10. The regions near the structure and the free surface are refined for better flow capture.

For the present investigation, the irregular wave with a significant

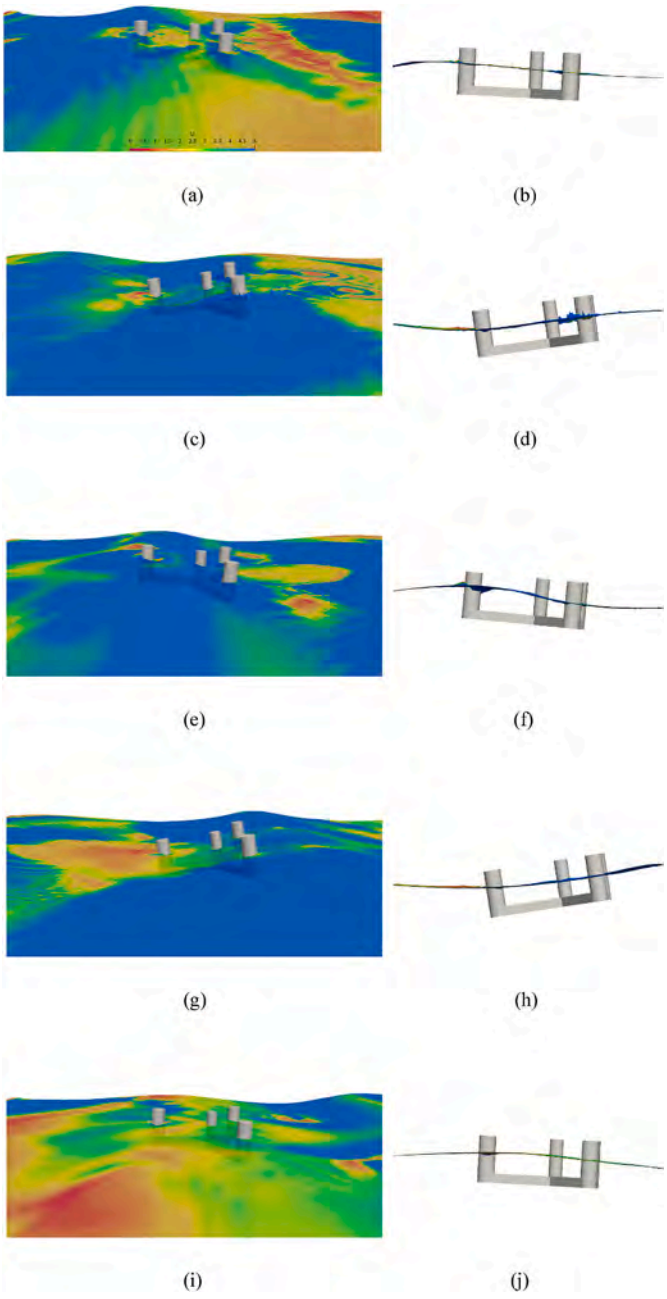

Fig. 12. Visualization of the VolturnUS-S semi-submersible platform dynamics under freak wave with a focusing crest amplitude of 12 m: (a) 3D and (b) side views at $t = 82.50$s; (c) 3D and (d) side views at $t = 89.75$s; (e) 3D and (f) side views at $t = 96.50$s; (g) 3D and (h) side views at $t = 104.00$s; (i) 3D and (j) side views at $t = 112.25$s.

height of 6 m and a peak period of 15s is used. Frequency range between 0.04 Hz and 0.20 Hz is discretized into 32 pieces for demonstrating the characteristics of the JONSWAP spectrum. The amplitude of each wave component is defined according to equation (40). The focusing time and location are 100s and 300 m, respectively. The phases are obtained for each wave using equation (44). Numerous test cases presented in Table 7 are carried out for the parameter study on the hydrodynamics of the UMaine VolturnUS-S semi-submersible platform under freak waves. Specifically, four factors, i.e., focusing crest amplitude, focusing location, angle of the platform relative to the incoming wave and location of center of gravity (COG) of the platform, are considered. The 0° angle is shown by Fig. 9(c) and (d) with the mooring line 1 aligned with the x axis. Positive angles are denoted by anti-clockwise rotation. The range of angle from 0° to 60° is investigated due to the symmetry of the platform.

6.3. Mesh convergence study

For the mesh convergence, three grids with total cells of 1,270,137, 2,674,663 and 3,794,245 are generated and the simulated results are shown in Fig. 11. The selected freak wave has a focusing crest amplitude of 12 m and the focusing occurs at the central column center at $t = 100$s. As shown by the figure, the medium and fine meshes give almost converged motion responses in heave and pitch. For the surge motion, the results with the three grids are generally identical before 120s but diverge after that time. Since only the platform responses near the focusing time $t = 100$s are concerned, the medium mesh which has a minimum cell side length of 0.5 m near the free surface and the structure is considered as sufficient for the present investigation purpose and is thus used for all the simulations. The calculated y^+ values over the platform hull are between 160.0 and 200.0 which stay in the range of the inertial sublayer. Note that the simulations are all performed in supercomputers, and each case demands about 200 h of computing time with 80 processors. Although CFD simulations demand significantly more computational cost comparing to the engineering models, the motion properties of structures as well as the flow characteristics can be well reproduced within CFD modeling which fulfils the purpose of the present investigation. Moreover, to study the effect of using the Mentor SST k - ω model for the turbulence modeling, the simulation with no turbulence model has been conducted. In Fig. 11, the curve marked with (Y) means that the turbulence model is used while the curve marked with (N) shows results obtained with no turbulence model. It is seen in the figure that almost identical results are obtained between the simulations with and without turbulence model.

7. Results and discussion

7.1. Description of the basic case

In the basic case, the focusing crest amplitude is 12 m which occurs at the centerline of the central column with an incidence angle of 0°. The dynamics of the VolturnUS-S platform under the basic loading is visualized in Fig. 12, and the motion responses and mooring line fairlead tensions are plotted in Fig. 13. The times in Fig. 12 correspond to the instants when the pitching angle reaches local maxima or minima, which are also highlighted by black vertical dash lines in Fig. 13(a) and (d) and red circles in the trajectories in Fig. 13(b) and (c).

Fig. 12(a) and (b) show that the platform positively pitches to a local peak when a wave crest arrives at the front column at around $t = 82.50$s. This wave impact leads to continuous rise in surge of the structure as it moves across the platform while the heaving motion first increases and then decreases with the local peak occurs later than that of the pitching motion (see Fig. 13(a)). The pitch of the platform reduces to a local minimum when the wave crest passes to the rear columns at $t = 89.75$s, and meanwhile, a wave trough approaches the front column as shown in Fig. 12(c) and (d). Fig. 13(a) indicates that the platform surges to the maximum horizontal position of the cycle at this moment. As the new wave trough propagates through the semi-submersible platform, the structure reverses motion in surge and continuously moves back till another wave crest reaches the front column at $t = 96.50$s when the pitch rises to local maximum again (see Fig. 12(e) and (f)). During this time, the structural elevation first lowers bottoming out as the wave trough arrives somewhere amid the platform and then rises along with the positive pitching motion. The roughly periodic motions repeat as new wave crest and trough propagate through the structure from $t = 96.50$s to $t = 112.25$s shown by Fig. 12(e)–(j). As the focusing phenomenon occurs during this period at $t = 100.00$s, the wave-structure interaction behaves the most severe. Local wave splashing around columns can be evidently observed in the subfigures. The motions in all the three DOFs undergo the largest variations as indicated in Fig. 13(a).

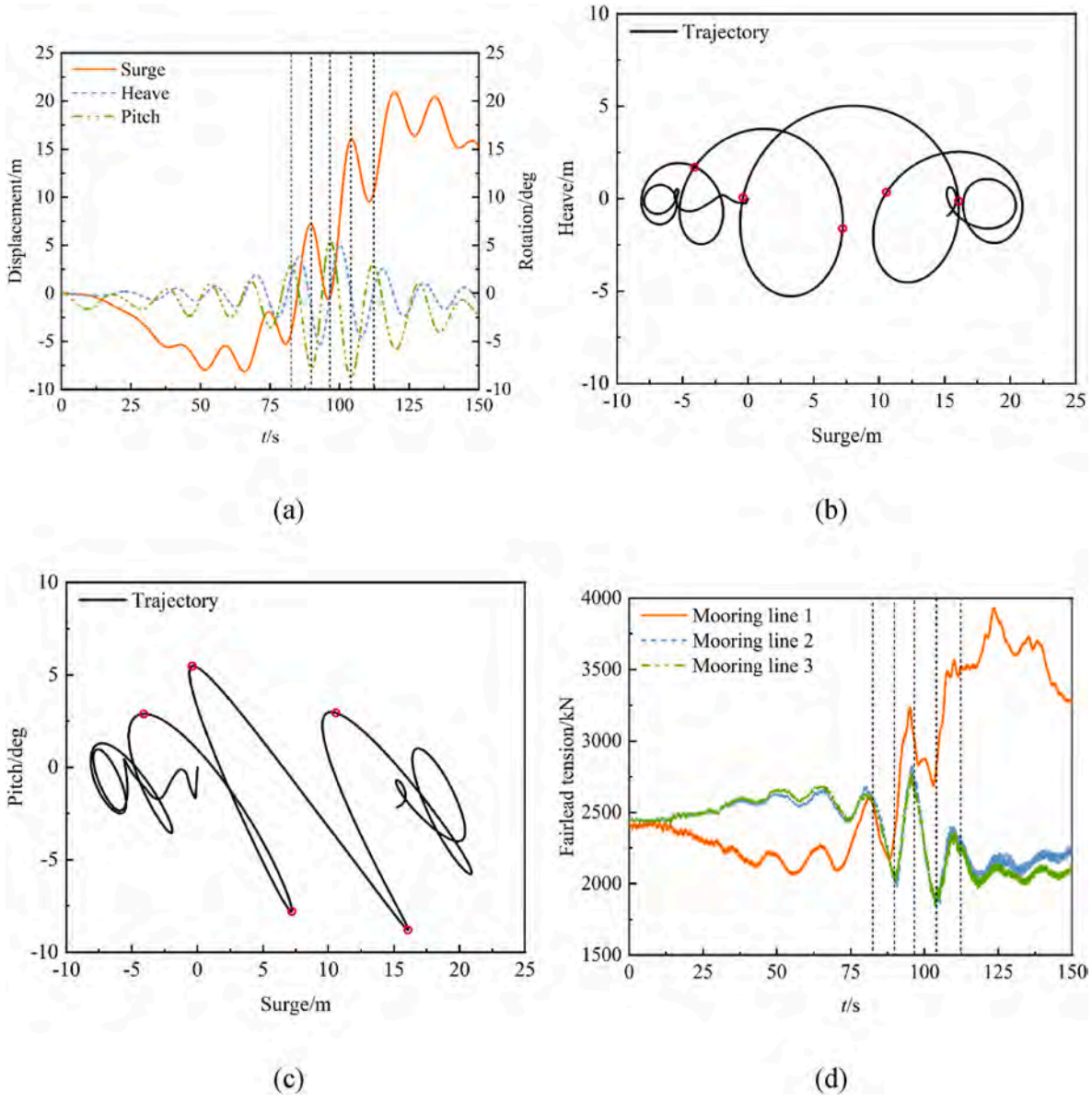

Fig. 13. Dynamic responses of the VolturnUS-S semi-submersible platform under freak wave with a focusing crest amplitude of 12 m: (a) Motion responses; (b) Trajectory in the surge and heave plane; (c) Trajectory in the surge and pitch plane; (d) Mooring line fairlead tensions.

Overall, Fig. 13(a) manifests that the platform oscillates about the mean position in heave and pitch following the wave with the amplitude dependent on the wave motion, while in the surge DOF, the platform oscillates with net shift over each cycle to move forward in the wave propagating direction. It is seen that the net shift in surge is positively related to the wave amplitude. Moreover, as already described on the platform dynamics in each oscillation cycle in Fig. 12, the heaving motion lags in phase comparing to the pitching motion, and there is a rough 180° phase difference between surge and pitch DOFs and a rough 90° phase difference between surge and heave DOFs. In specific, when the motion in surge reaches a local maximum, the pitch DOF is in its local minimum and the heave DOF is at around its mean position moving toward to its minimum. These features are intuitively demonstrated in Fig. 13(b) and (c), in which the times when the pitching motion is maximum or minimum are marked with red circles corresponding to the time sequence in Fig. 12. Fig. 13(c) reveals that the rotational recovery from minimum pitch is sharper than that from maximum pitch during each oscillation cycle for the surge-pitch coupled movement. These coupled motion characteristics between DOFs should be considered for wind turbine aerodynamic designs.

The fairlead tensions at the three mooring lines are drawn in Fig. 13 (d). The numbering scheme for the mooring system is shown by Fig. 9. It is seen that the fairlead tensions at all mooring lines oscillate with the platform motions. The fairlead tensions at the mooring line 2 and 3 are generally identical due to the symmetry of the configuration, and decrease to lower values than the initial values after the wave focusing occurs. In contrast, the mooring line 1 which links to the front column increases significantly in fairlead tension due to the dramatic forward surge motion of the platform. This boosts requirements for the mooring line ultimate strength to bear the loading under freak waves.

7.2. *Effect of focusing crest amplitude*

Freak waves with three different amplitudes impacting on the VolturnUS-S platform are simulated to assess the effect of focusing crest amplitude (See Table 7). The amplitudes of wave components are computed by equation (40) according to the desired crest value while the phase shift values are the same as the basic case for consistent

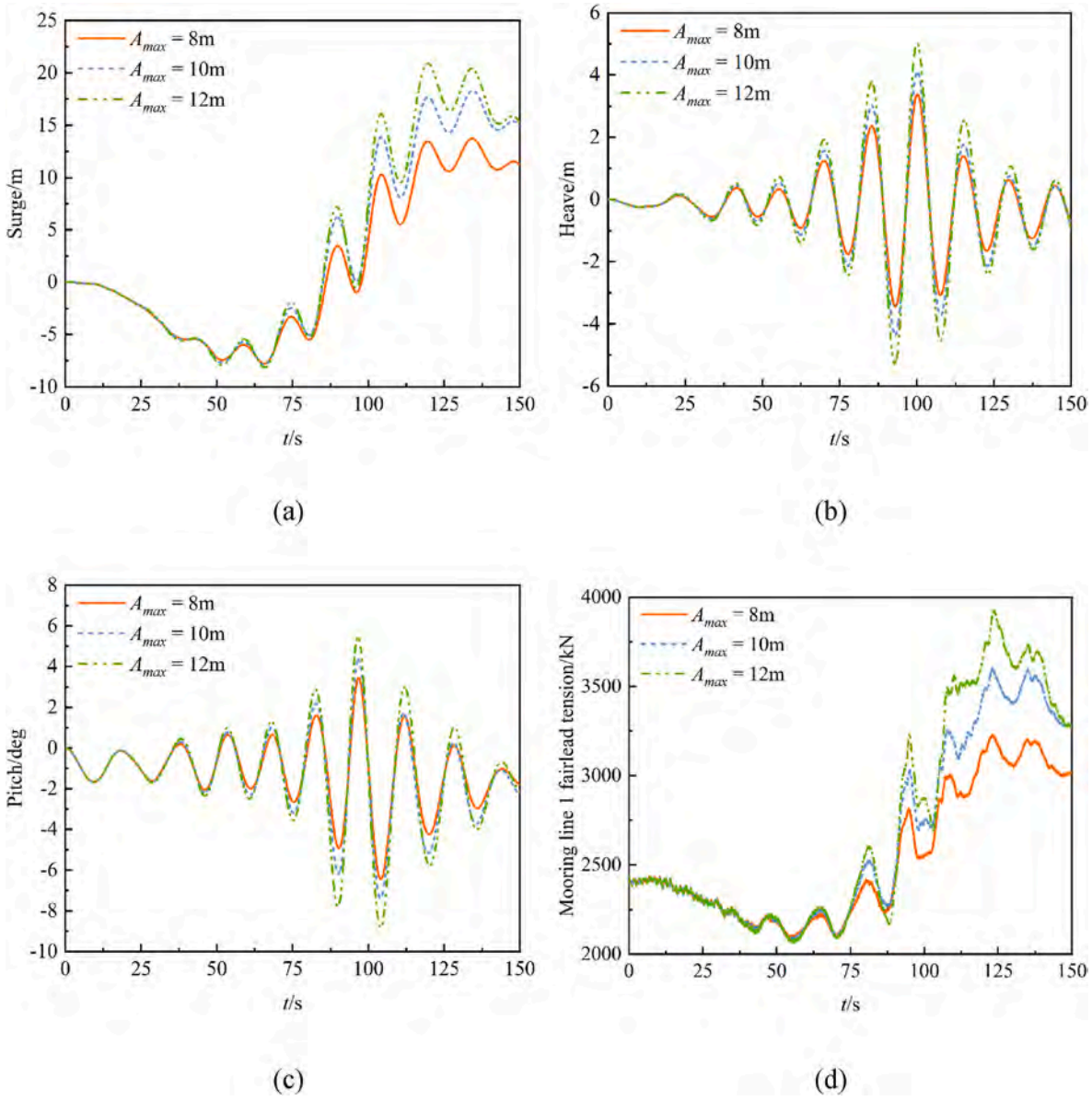

Fig. 14. Dynamic responses of the VolturnUS-S semi-submersible platform under freak waves with different focusing crest amplitudes: (a) Surge motion; (b) Heave motion; (c) Pitch motion; (d) Mooring line 1 fairlead tensions.

temporal and spatial focusing. The platform motion and mooring line 1 fairlead tension results are shown in Fig. 14. It is shown that the dynamic behaviors of the structure have similar features across the three wave conditions, and enhance in magnitude with the focusing crest amplitude. This is consistent with Deng et al. (2017). Moreover, the enhancement from A_{max} = 8 m wave case to A_{max} = 10 m wave case is greater than that from A_{max} = 10 m wave case to A_{max} = 12 m wave case especially in surge motion and mooring line 1 fairlead tension. This implies the nonlinearity of the system resulted from the wave-structure interaction and mooring dynamics. Apparently, with higher mooring line tension under stronger wave impact, the ease to move the platform is weakened leading to increasing nonlinearity in the wave-structure interaction. It is also noted that the maximum focusing crest amplitude considered in the present study is 12 m which is close to the freeboard length (15 m) of the VolturnUS-S platform (See Fig. 9(b)). Due to the heave motion which reaches about 5 m under wave impact, the platform deck is well safe from wave slamming. It is anticipated that as the focusing crest amplitude rises to a sufficiently high value, the platform with motion restricted by the mooring system would be submerged during wave crest passage, and in this case, different characteristics in wave-structure interaction will be demonstrated.

7.3. *Effect of focusing location*

The effect of focusing location of freak waves on the dynamics of the platform is analyzed. Seven focusing locations are considered, including −51.75 m, −34.50 m, −17.25 m, 0.00 m, 17.25 m, 34.50 m and 51.75 m from the platform initial position. Fig. 15 shows the simulation results of the motion and mooring line fairlead tension responses. It is seen that changing the focusing location affects both the variation amplitudes and phases of the structural dynamics. Comparing to the effect of focusing crest amplitude illustrated by Fig. 14, the change in focusing location has smaller effect on modifying the platform motion amplitude. This means that when a freak wave occurs nearby, its effect on the dynamics of the structure will always be significant regardless of the exact focusing location. Moreover, the change in structural motion phase with the focusing location reflects the change in spatial relation between the wave and structural components of the platform. It is also observed in

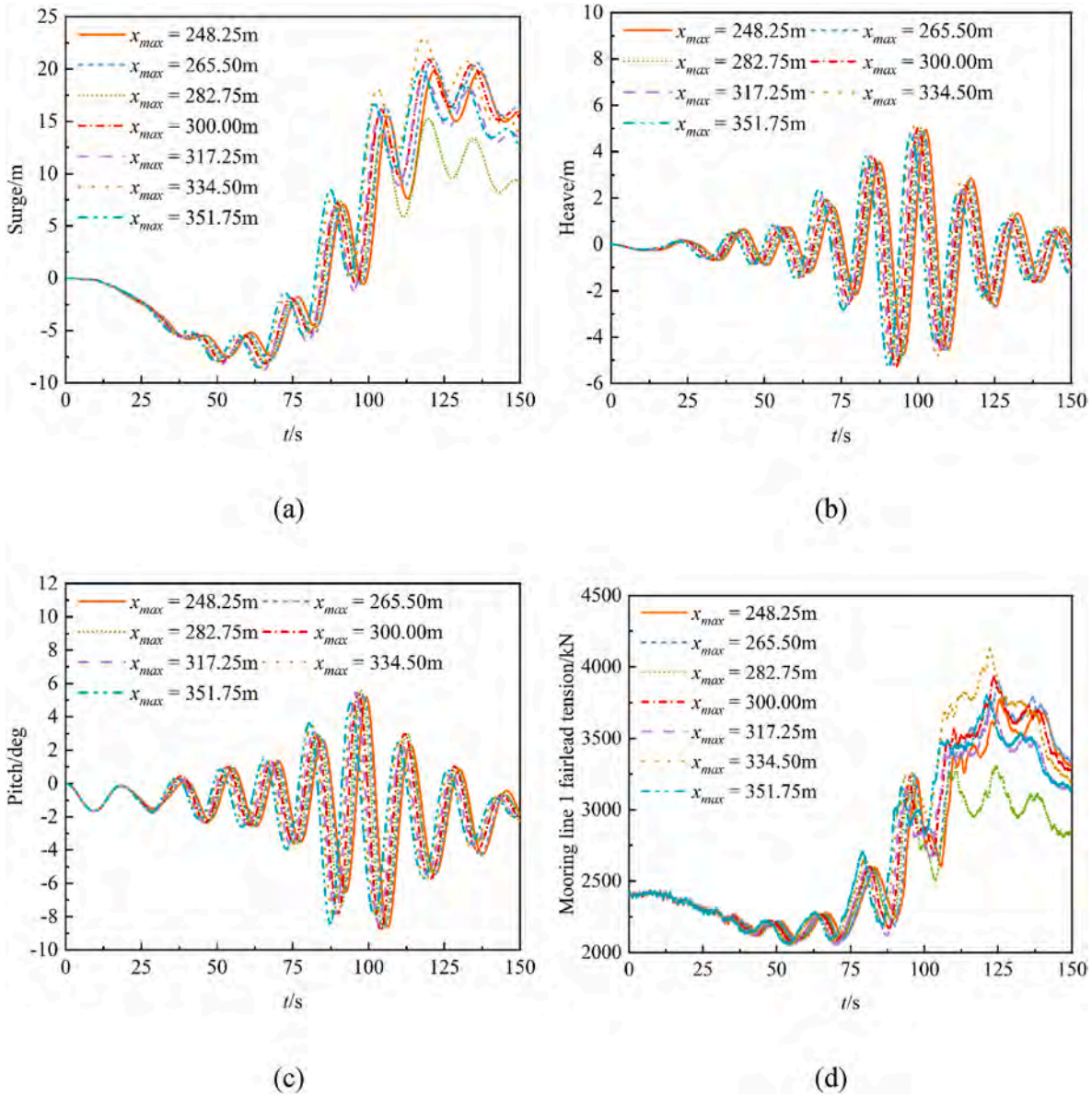

Fig. 15. Dynamic responses of the VolturnUS-S semi-submersible platform under freak waves with different focusing locations: (a) Surge motion; (b) Heave motion; (c) Pitch motion; (d) Mooring line 1 fairlead tensions.

Fig. 15 that with the focusing relocated, the phases of all dynamic quantities vary in the same manner.

7.4. Effect of incident angle

The behavior of the wave-structure interaction under freak waves changes with the wave as well as the structural configuration. Cleary and Rudman (2009) found that the characteristics of the semi-submersible platform motion responses under extreme waves are affected by the type of the mooring system. For the TLP system, the surge motion is small but the heave motion is significant, while for TSM with lines angled 45° against the ocean floor, the reverse is true. Rudman and Cleary (2013) gave detailed analysis on the effects of incident angle and mooring line pretension on the dynamics of a semi-submersible platform under rogue waves. In this section, the effect of freak wave incident angle on the platform dynamics is analyzed. Five angles of attack, i.e., 0°, 15°, 30°, 45° and 60°, are considered due to the symmetry of the platform column arrangements (see Table 7). The positive rotation direction is anti-clockwise when looking from top as seen in Fig. 9(c). The motion and mooring line fairlead tension results are shown in Figs. 16 and 17, respectively.

It is seen in Fig. 16(a) that the surge response reduces significantly as the wave incident angle increases from 0° to 30° and varies slightly between 30° and 60°. The reduction in surge is somehow compensated by increase in sway. As seen in Fig. 16(b), the least sway motion is present when the incident angle is 0°. Significant increase in sway is obtained as the wave incident angle varies from 0° to 30°. Different from surge responses which oscillate with the wave, the platform sways in a simple movement. The sway motion is considered as due to the unbalanced forces on the three corner columns in the cross-flow direction and restoration from the mooring lines. Since the rotation angle 30°corresponds to the maximum unbalance where the mooring line 2 is aligned with the y axis, the surge and sway motion variations as the wave incident angle changes from 0° to 30° are the most significant. It is noted that the sway motion reaches high values even when the platform configuration is symmetric at the wave incident angle of 60°, which is contributed by the offset mass center of the whole FOWT system toward the mooring line 1. Fig. 16(c) shows that the heave motion varies

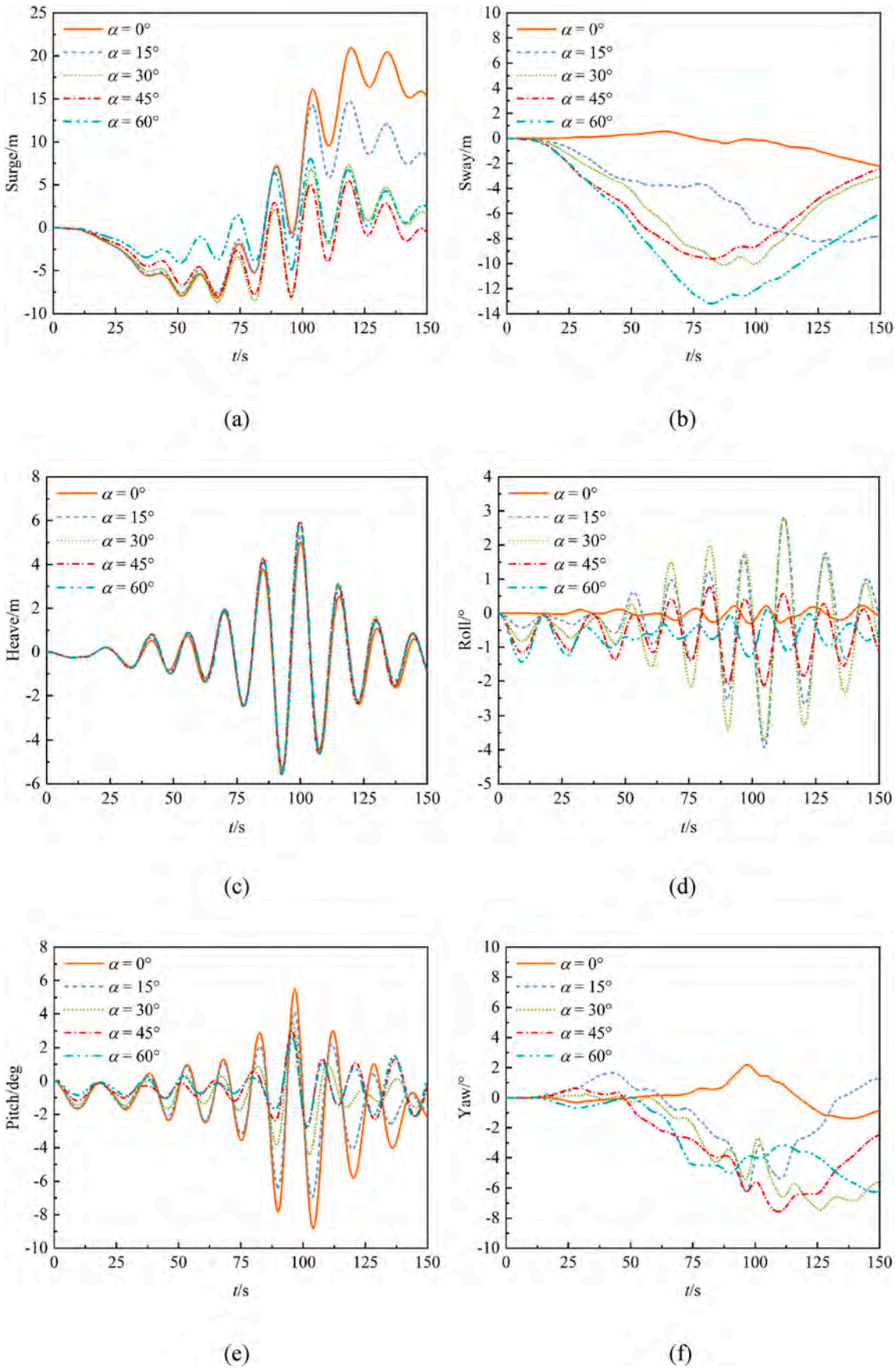

Fig. 16. Motion responses of the VolturnUS-S semi-submersible platform under freak waves with different incident angles: (a) Surge motion; (b) Sway motion; (c) Heave motion; (d) Roll motion; (e) Pitch motion; (f) Yaw motion.

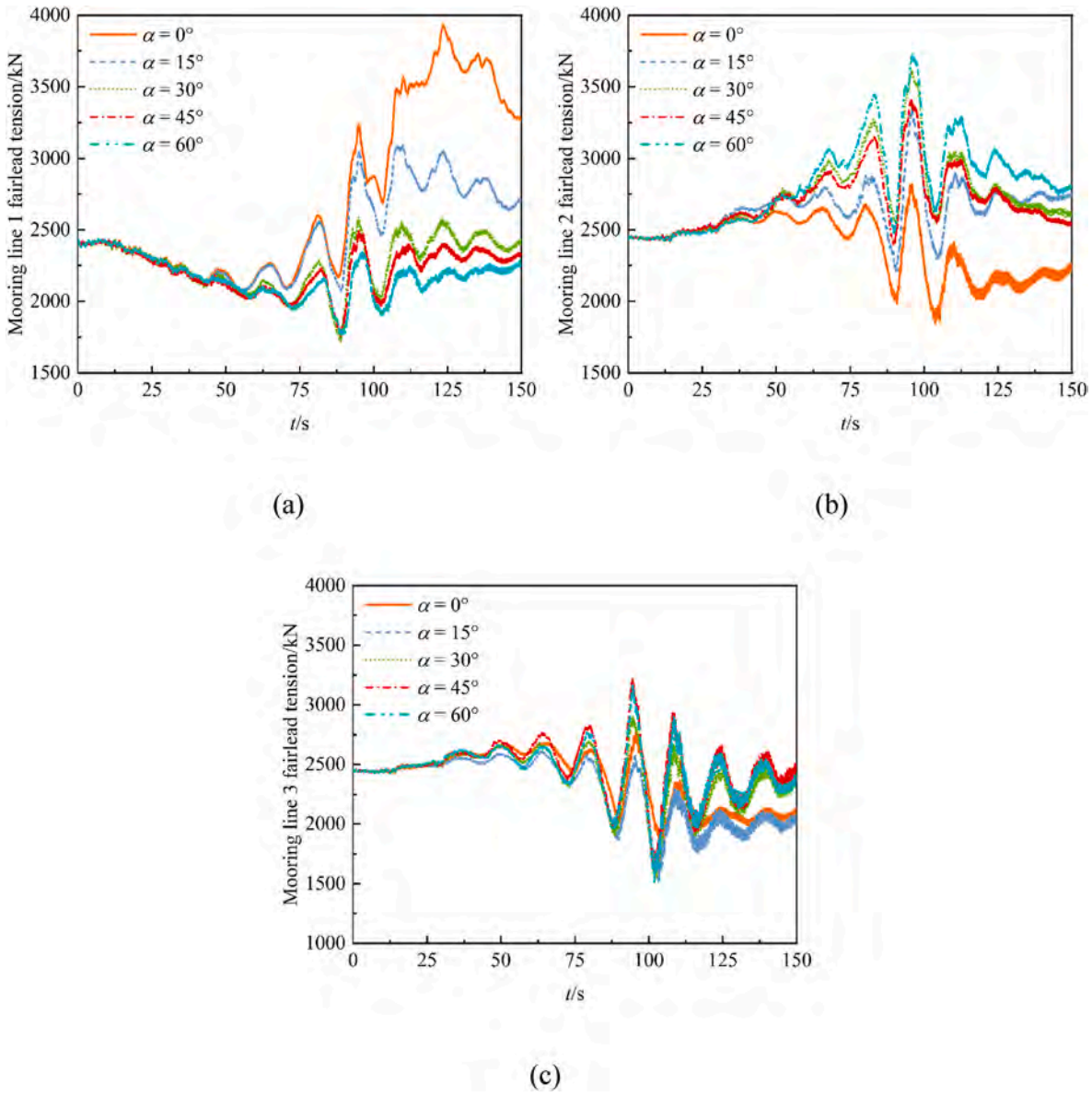

Fig. 17. Mooring line fairlead tensions of the VolturnUS-S semi-submersible platform under freak waves with different incident angles: (a) Mooring line 1; (b) Mooring line 2; (c) Mooring line 3.

slightly with the wave incident angle. For the roll motion shown in Fig. 16(d), the least response amplitude occurs at the wave incident angle of 0°, and the largest response amplitude occurs at the wave incident angle of 30° when the platform is the most unbalanced relative to the wave. At the wave incident angle of 60°, the roll oscillation is more significant than that of 0° angle which is due to the offset mass center. Fig. 16(e) indicates that the pitch response is the most dramatic at the wave incident angle of 0° and reduces to a low level at wave incident angles from 30° to 60°. This is due to the restoration from mooring lines since there is only one upstream mooring line at the wave angles from 0° to 30° and one more mooring line joins the upstream region when the wave incident angle exceeds 30°. The yaw motion response shown in Fig. 16(f) increases with the wave incident angle which is again due to the unbalanced forces from the wave. A visual comparison of the platform motion responses with different incident angles at around the time of maximum positive pitch is shown in Fig. 18.

Fig. 17 manifests that the most benefit from the platform rotation is the extreme fairlead tension reduction in mooring line 1. This only upstream mooring line reduces significantly in extreme fairlead tension as the wave incident angle varies from 0° to 30°. After that, one more upstream mooring line joins, and the fairlead tension in mooring line 1 continues to decrease from angle 30° to angle 60° but with smaller effect. In contrast, the fairlead tension in mooring line 2 continuously increase in oscillation amplitude as the wave incident angle varies from 0° to 60°. The fairlead tension in mooring line 3 varies relatively gently among the incident angles.

7.5. *Effect of gravity center location*

In the above sections, the COG of the complete FOWT system is set at (−0.2 m, −2.2 m) which considers the effect of the mounted wind turbine and reflects an inherent mass center offset toward the mooring line 1. In this section, three preset COG locations along the centerline of the central column are examined to reveal its the impact. The motion and mooring line fairlead tension responses of the platform are presented in Fig. 19.

It is seen in Fig. 19(a) and (d) that moving COG to the centroid of the horizontal geometry of the platform configuration drastically reduces

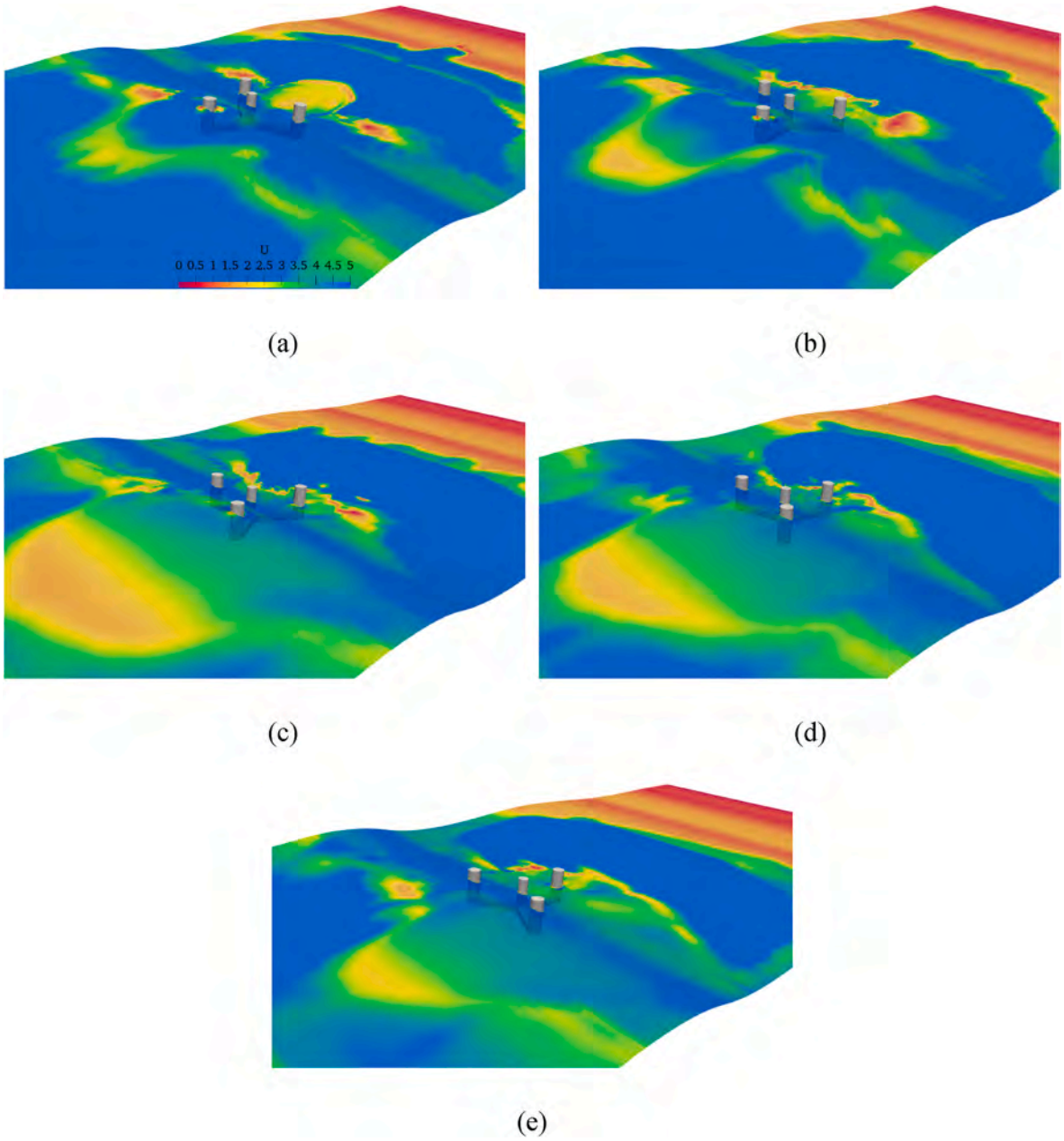

Fig. 18. Visual comparison of the VolturnUS-S semi-submersible platform dynamics under freak waves with different incident angles at around the time of maximum positive pitch: (a) $\alpha = 0^\circ$ ($t = 96.50$s); (b) $\alpha = 15^\circ$ ($t = 96.50$s); (c) $\alpha = 30^\circ$ ($t = 96.00$s); (d) $\alpha = 45^\circ$ ($t = 95.50$s); (e) $\alpha = 60^\circ$ ($t = 95.50$s).

the extreme surge displacement and upstream mooring line fairlead tension while its impacts on the variation amplitude over each oscillation cycle are relatively small. In other words, large net shift in surge over each oscillation cycle is eliminated for a completely axisymmetric FOWT system. It is expected that with an offset mass center, the platform inclines to obtain equilibrium from the initial vertical gesture causing the restorative forces of the three mooring lines unbalanced in the horizontal plane, which is the reason for the negative surge motion during the first 75s of the simulation for the basic case. Fig. 19(a) shows that during the wave focusing event, the semi-submersible platform with offset mass center gains more forward momentum via interacting with the freak wave while modest wave-structure interactions occur for other configurations. This is regarded as the results of different spatial relations between the crest of the focused wave and the platform. For the case with offset mass center, the platform is situated in a more preferrable way, i.e., having a distance from the wave crest, for the focused wave to push it forward, while for the other cases, the platform oscillates to near the wave crest when the wave focuses. The offset of mass center also affects the pitching responses. It is seen in Fig. 19(c) that with the mass center moved upstream, the platform pitches back and forth once the simulation starts, and the mean orientation tilts negative. The amplitude of the pitching response during the wave focusing varies slightly with the COG relocation. Fig. 19(b) indicates that the effect of changing the COG location on the platform heave motion response is small.

In addition, it is seen in Fig. 19 that when COG is placed along the centerline of the central column, modification of its elevation causes small variations to both the motion and mooring line fairlead tension responses of the platform. No obvious variation trends of the responses in surge and heave DOFs and mooring line 1 fairlead tension with COG height are demonstrated. But the response in pitch DOF enhances as COG lowers its vertical position. It is due to the shortened distance between COG and center of buoyancy (COB) as COG goes down which leads to reduction in the restoring moment contribution from buoyancy.

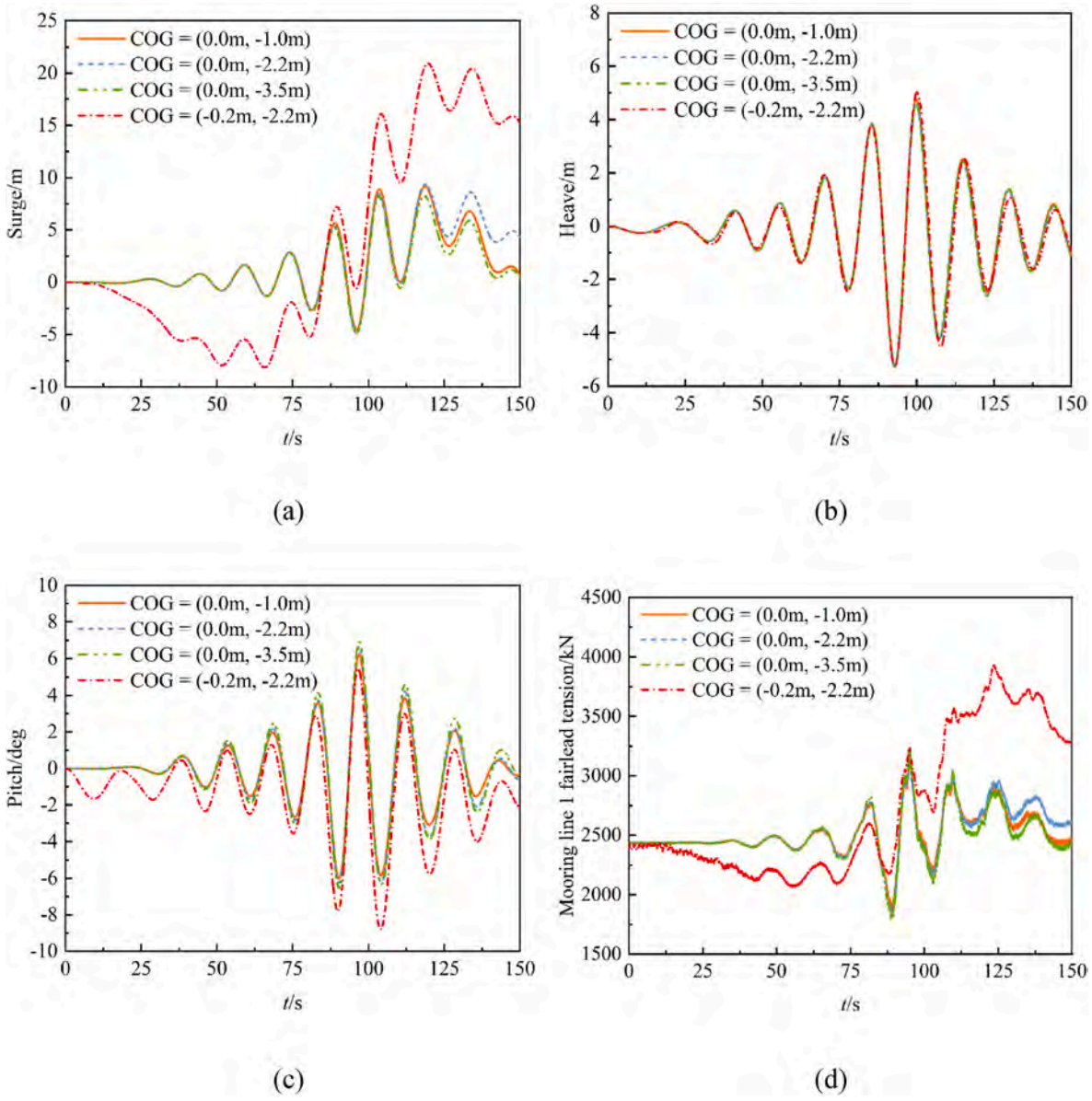

Fig. 19. Dynamic responses of the VolturnUS-S semi-submersible platform under freak waves with different COG locations: (a) Surge motion; (b) Heave motion; (c) Pitch motion; (d) Mooring line 1 fairlead tensions.

This reflects the design philosophy of semi-submersible type floating structures which gain stability through distributed buoyancy taking advantage of weighted water plane area for righting moment.

8. Conclusions

In this study, a coupled CFD and dynamic mooring line model for the hydrodynamics of FOWTs was presented. The mooring line module adopts a dynamic approach with LDG FEM discretization. Details of the models used in the coupled hydrodynamic-mooring analysis and the coupling schemes between CFD, rigid body dynamics and mooring model were described. To validate the coupled model, free-decay tests and motion responses under regular waves of the DeepCwind semi-submersible platform were simulated. Results show that the coupled CFD and mooring line model is accurate with respect to the experiment data and exhibits greater reliability than the model-based approach. The CFD-mooring model was then used to study the dynamics of the UMaine VolturnUS-S semi-submersible platform designed for supporting the IEA 15 MW wind turbine under freak waves. The NewWave theory which describes the surface elevation and velocity of a focused group of localized waves was used for wave generation. A detailed parametric analysis on the wave-structure interaction problem has been conducted. The main conclusions are summarized in the following.

1. Under the freak wave, the semi-submersible platform oscillates about the mean position in heave and pitch DOFs with the amplitude dependent on the wave motion, while in the surge DOF, the platform oscillates with net shift over each cycle to move forward a long distance away from the initial position. The heaving motion lags in phase than the pitching motion, and there is a rough 180° phase difference between surge and pitch DOFs and a rough 90° phase difference between surge and heave DOFs. The fairlead tensions in all mooring lines oscillate with the platform motions. Particularly, the fairlead tension in the upstream mooring line soars due to the dramatic forward surge motion of the platform.
2. For the three focusing crest amplitudes considered, the dynamic behaviors of the semi-submersible platform show similar features, and enhance with the amplitude. The nonlinearity of the system

resulted from the wave-structure interaction and mooring dynamics shows stiffer effect with higher focusing crest amplitude especially demonstrated by the surge motion and upstream mooring line fairlead tension responses.

3. Comparing to the effect of focusing crest amplitude, the change in focusing location has smaller effect on modifying the platform motion amplitude. Relocating the focusing event also alters the spatial relation between the wave and structural components of the platform, leading to variations in the phases of the structural dynamics.
4. The surge response of the semi-submersible platform reduces significantly as the wave incident angle increases from 0° to 30° and varies slightly between 30° and 60°. In the sway DOF, the least motion is present when the incident angle is 0°, and significant rise in response is obtained as the wave incident angle varies from 0° to 30°. The heave motion varies slightly with the wave incident angle. For the roll motion, the least response amplitude occurs at the wave incident angle of 0°, and the largest response amplitude occurs at the wave incident angle of 30° when the platform is the most unbalanced relative to the wave. The pitch response is the most dramatic at the wave incident angle of 0° and reduces to a low level at wave incident angles from 30° to 60°. The yaw motion response increases with the wave incident angle which is again due to the unbalanced forces from the wave. The most benefit from the platform rotation is the extreme fairlead tension reduction in the upstream mooring system as the wave incident angle varies from 0° to 60°.
5. The extreme surge displacement and upstream mooring line fairlead tension of the semi-submersible platform reduce drastically when COG is moved to the centroid of the platform horizontal geometry. The upstream offset of mass center causes the platform to pitch back and forth from the beginning of simulations, and the mean orientation to tilt negative. The effect of changing the COG location on the platform heave motion is small. When COG is placed along the centerline of the central column, lowering COG enhances the motion response in pitch DOF.

CRediT authorship contribution statement

Wenjie Zhong: Data curation, Writing – original draft preparation, Visualization, Investigation, Software, Validation.Xiaoming Zhang: Investigation, Validation.Decheng Wan: Supervision, Conceptualization, Methodology, Investigation, Writing-Reviewing and Editing

Funding

National Natural Science Foundation of China (52101324, 52131102), the National Key Research and Development Program of China (2019YFB1704200).

Declaration of competing interest

The authors declare that they have no known competing financial interests or personal relationships that could have appeared to influence the work reported in this paper.

Data availability

Data will be made available on request.

Acknowledgement

This work is supported by the National Natural Science Foundation of China (52101324, 52131102), the National Key Research and Development Program of China (2019YFB1704200), to which the authors are most grateful.

References

Allen, C., Viscelli, A., Dagher, H., Goupee, A., Gaertner, E., Abbas, N., Hall, M., Barter, G., 2020. Definition of the UMaine VolturnUS-S Reference Platform Developed for the IEA Wind 15-megawatt Offshore Reference Wind Turbine (No.). National Renewable Energy Lab. (NREL), Golden, CO (United States); University of Maine, Orono. ME (United States), NREL/TP-5000-76773.

Antonutti, R., Peyrard, C., Incecik, A., Ingram, D., Johanning, L., 2018. Dynamic mooring simulation with Code_Aster with application to a floating wind turbine. Ocean Eng. 151, 366–377.

Antonutti, R., Peyrard, C., Johanning, L., Incecik, A., Ingram, D., 2016. The effects of wind-induced inclination on the dynamics of semi-submersible floating wind turbines in the time domain. Renew. Energy 88, 83–94.

Belytschko, T., Liu, W.K., Moran, B., Elkhodary, K., 2014. Nonlinear Finite Elements for Continua and Structures. John wiley & sons.

Berberovic, E., van Hinsberg, N.P., Jakirlic, S., Roisman, I.V., Tropea, C., 2009. Drop impact onto a liquid layer of finite thickness: dynamics of the cavity evolution. Phys. Rev. 79 (3), 36306, 36306.

Bertotti, L., Cavaleri, L., 2008. Analysis of the Voyager storm. Ocean Eng. 35 (1), 1–5.

Carrion, M., Steijl, R., Woodgate, M., Barakos, G.N., Munduate, X., Gomez-Iradi, S., 2014. Aeroelastic analysis of wind turbines using a tightly coupled CFD-CSD method. J. Fluid Struct. 50, 392–415.

Chandrasekaran, S., Yuvraj, K., 2013. Dynamic analysis of a tension leg platform under extreme waves. J. Nav. Architect. Mar. Eng. 10 (1), 59–68.

Chen, L., Basu, B., Nielsen, S.R., 2018. A coupled finite difference mooring dynamics model for floating offshore wind turbine analysis. Ocean Eng. 162, 304–315.

Cheng, P., Huang, Y., Wan, D., 2019. A numerical model for fully coupled aero-hydrodynamic analysis of floating offshore wind turbine. Ocean Eng. 173, 183–196.

Clauss, G.F., 2002. Dramas of the sea: episodic waves and their impact on offshore structures. Appl. Ocean Res. 24 (3), 147–161.

Cleary, P.W., Rudman, M., 2009. Extreme wave interaction with a floating oil rig: prediction using SPH. Prog. Comput. Fluid Dynam. Int. J. 9 (6–7), 332–344.

Cockburn, B., Shu, C.W., 1998. The local discontinuous Galerkin method for time-dependent convection-diffusion systems. SIAM J. Numer. Anal. 35 (6), 2440–2463.

Coulling, A.J., Goupee, A.J., Robertson, A.N., Jonkman, J.M., Dagher, H.J., 2013. Validation of a FAST semi-submersible floating wind turbine numerical model with DeepCwind test data. J. Renew. Sustain. Energy 5 (2), 023116.

Dai, J., Hu, W., Yang, X., Yang, S., 2018. Modeling and investigation of load and motion characteristics of offshore floating wind turbines. Ocean Eng. 159, 187–200.

Deng, Y., Yang, J., Xiao, L., 2014. Influence of wave group characteristics on the motion of a semisubmersible in freak waves. In: International Conference on Offshore Mechanics and Arctic Engineering, vol. 45370. American Society of Mechanical Engineers, V01AT01A045.

Deng, Y., Yang, J., Zhao, W., Xiao, L., Li, X., 2017. Surge motion of a semi-submersible in freak waves. Ships Offshore Struct. 12 (4), 443–451.

Dysthe, K., Krogstad, H.E., Muller, P., 2008. Oceanic rogue waves. Annu. Rev. Fluid Mech. 40, 287–310.

Gaertner, E., Rinker, J., Sethuraman, L., Zahle, F., Anderson, B., Barter, G., Abbas, N., Meng, F., Bortolotti, P., Skrzypinski, W., Scott, G., Feil, R., Bredmose, H., Dykes, K., Shields, M., Allen, C., Viselli, A., 2020. IEA Wind TCP Task 37: Definition of the IEA 15-Megawatt Offshore Reference Wind Turbine. National Renewable Energy Lab. (NREL), Golden, CO (United States). NREL/TP-5000-75698.

Hall, M., Buckham, B., Crawford, C., 2014. Evaluating the importance of mooring line model fidelity in floating offshore wind turbine simulations. Wind Energy 17 (12), 1835–1853.

Hasselmann, K., Barnett, T.P., Bouws, E., Carlson, H., Cartwright, D.E., Enke, K., Ewing, J.A., Gienapp, A., Hasselmann, D.E., Kruseman, P., Meerburg, A., Muller, P., Olbers, D.J., Richter, K., Sell, W., Walden, H., 1973. Measurements of Wind-Wave Growth and Swell Decay during the Joint North Sea Wave Project (JONSWAP). Ergaenzungsheft zur Deutschen Hydrographischen Zeitschrift, Reihe A.

Higuera, P., Lara, J.L., Losada, I.J., 2013. Realistic wave generation and active wave absorption for Navier-Stokes models: application to OpenFOAM. Coast. Eng. 71, 102–118.

Hirt, C.W., Nichols, B.D., 1981. Volume of fluid (VOF) method for the dynamics of free boundaries. J. Comput. Phys. 39 (1), 201–225.

Huang, Y., Cheng, P., Wan, D., 2019. Numerical analysis of a floating offshore wind turbine by coupled aero-hydrodynamic simulation. J. Mar. Sci. Appl. 18, 82–92.

Huang, Y., Zhuang, Y., Wan, D., 2021. Hydrodynamic study and performance analysis of the OC4-DeepCwind platform by CFD method. Int. J. Comput. Methods 18 (4), 2050020.

Jonkman, J.M., 2009. Dynamics of offshore floating wind turbines-model development and verification. Wind Energy 12 (5), 459–492.

Koo, B.J., Goupee, A.J., Kimball, R.W., Lambrakos, K.F., 2014. Model tests for a floating wind turbine on three different floaters. J. Offshore Mech. Arctic Eng. 136 (2).

Kvittem, M.I., Moan, T., 2015. Time domain analysis procedures for fatigue assessment of a semi-submersible wind turbine. Mar. Struct. 40, 38–59.

Lee, K., Huque, Z., Kommalapati, R., Han, S.E., 2017. Fluid-structure interaction analysis of NREL phase VI wind turbine: aerodynamic force evaluation and structural analysis using FSI analysis. Renew. Energy 113, 512–531.

Lehner, S., Rosenthal, W., 2006. Investigation of ship and platform accidents due to severe weather events: results of the Maxwave project. In: International Conference on Offshore Mechanics and Arctic Engineering, vol. 47489, pp. 753–760.

Li, L., Liu, Y., Yuan, Z., Gao, Y., 2019. Dynamic and structural performances of offshore floating wind turbines in turbulent wind flow. Ocean Eng. 179, 92–103.

Lin, Z., Qian, L., Bai, W., 2021. A coupled overset CFD and mooring line model for floating wind turbine hydrodynamics. In: The 31st International Ocean and Polar Engineering Conference. OnePetro.
Liu, Y., Li, S., Yi, Q., Chen, D., 2016. Developments in semi-submersible floating foundations supporting wind turbines: a comprehensive review. Renew. Sustain. Energy Rev. 60, 433–449.
Liu, Y., Xiao, Q., Incecik, A., Peyrard, C., Wan, D., 2017. Establishing a fully coupled CFD analysis tool for floating offshore wind turbines. Renew. Energy 112, 280–301.
Liu, Y., Xiao, Q., Incecik, A., Peyrard, C., 2019. Aeroelastic analysis of a floating offshore wind turbine in platform-induced surge motion using a fully coupled CFD-MBD method. Wind Energy 22 (1), 1–20.
Luan, C., Gao, Z., Moan, T., 2017. Development and verification of a time-domain approach for determining forces and moments in structural components of floaters with an application to floating wind turbines. Mar. Struct. 51, 87–109.
Luan, C., Gao, Z., Moan, T., 2013. Modelling and analysis of a semi-submersible wind turbine with a central tower with emphasis on the brace system. In: International Conference on Offshore Mechanics and Arctic Engineering, vol. 55423. American Society of Mechanical Engineers, V008T09A024.
Masciola, M., Robertson, A., Jonkman, J., Coulling, A., Goupee, A., 2013. Assessment of the importance of mooring dynamics on the global response of the DeepCwind floating semisubmersible offshore wind turbine. In: The Twenty-Third International Offshore and Polar Engineering Conference. OnePetro.
Moukalled, F., Mangani, L., Darwish, M., 2015. The Finite Volume Method in Computational Fluid Dynamics: an Advanced Introduction with OpenFOAM and Matlab. Springer Publishing Company Incorporated.
Ning, D.Z., Zang, J., Liu, S.X., Taylor, R.E., Teng, B., Taylor, P.H., 2009. Free-surface evolution and wave kinematics for nonlinear uni-directional focused wave groups. Ocean Eng. 36 (15–16), 1226–1243.
Ong, M.C., Kamath, A., Bihs, H., Afzal, M.S., 2017. Numerical simulation of free-surface waves past two semi-submerged horizontal circular cylinders in tandem. Mar. Struct. 52, 1–14.
Palm, J., Eskilsson, C., Bergdahl, L., 2017. An hp-adaptive discontinuous Galerkin method for modelling snap loads in mooring cables. Ocean Eng. 144, 266–276.
Robertson, A., Jonkman, J., Vorpahl, F., Popko, W., Qvist, J., Froyd, L., Chen, X., Azcona, J., Uzunoglu, E., Guedes Soares, C., Luan, C., 2014. Offshore code comparison collaboration continuation within IEA wind task 30: phase II results regarding a floating semisubmersible wind system. In: International Conference on Offshore Mechanics and Arctic Engineering, vol. 45547. American Society of Mechanical Engineers, V09BT09A012.
Robertson, A.N., Wendt, F., Jonkman, J.M., Popko, W., Dagher, H., Gueydon, S., Qvist, J., Vittori, F., Azcona, J., Uzunoglu, E., Soares, C.G., 2017. OC5 project phase II: validation of global loads of the DeepCwind floating semisubmersible wind turbine. Energy Proc. 137, 38–57.
Roy, S., Ghosh, V., Dey, S., Vimmadi, S., Banik, A.K., 2017. A coupled analysis of motion and structural responses for an offshore spar platform in irregular waves. Ships Offshore Struct. 12, S296–S304.
Rudman, M., Cleary, P.W., 2013. Rogue wave impact on a tension leg platform: the effect of wave incidence angle and mooring line tension. Ocean Eng. 61, 123–138.
Rudman, M., Cleary, P.W., 2016. The influence of mooring system in rogue wave impact on an offshore platform. Ocean Eng. 115, 168–181.
Rusche, H., 2003. Computational Fluid Dynamics of Dispersed Two-phase Flows at High Phase Fractions, Doctoral Dissertation. Imperial College London (University of London).
Tran, T.T., Kim, D.H., 2015. The coupled dynamic response computation for a semi-submersible platform of floating offshore wind turbine. J. Wind Eng. Ind. Aerod. 147, 104–119.
Tran, T.T., Kim, D.H., 2016a. A CFD study into the influence of unsteady aerodynamic interference on wind turbine surge motion. Renew. Energy 90, 204–228.
Tran, T.T., Kim, D.H., 2016b. Fully coupled aero-hydrodynamic analysis of a semi-submersible FOWT using a dynamic fluid body interaction approach. Renew. Energy 92, 244–261.
Wang, W., Kamath, A., Pakozdi, C., Bihs, H., 2019. Investigation of focusing wave properties in a numerical wave tank with a fully nonlinear potential flow model. J. Mar. Sci. Eng. 7 (10), 375.
Westphalen, J., Greaves, D.M., Williams, C.J.K., Hunt-Raby, A.C., Zang, J., 2012. Focused waves and wave-structure interaction in a numerical wave tank. Ocean Eng. 45, 9–21.
Yan, J., Korobenko, A., Deng, X., Bazilevs, Y., 2016. Computational free-surface fluid-structure interaction with application to floating offshore wind turbines. Comput. Fluid 141, 155–174.
Yilmaz, O., Incecik, A.J.O.E., 1996. Extreme motion response analysis of moored semi-submersibles. Ocean Eng. 23 (6), 497–517.
Zhao, X., Hu, C., 2012. Numerical and experimental study on a 2-D floating body under extreme wave conditions. Appl. Ocean Res. 35, 1–13.
Zhong, W., Yim, S.C., Deng, L., 2020a. Vortex shedding patterns past a rectangular cylinder near a free surface. Ocean Eng. 200, 107049.
Zhong, W., Yim, S.C., Deng, L., 2020b. Reynolds-number effect on flow past a rectangular cylinder in the presence of a free surface. Ocean Eng. 216, 107865.
Zhou, Y., Xiao, Q., Liu, Y., Incecik, A., Peyrard, C., Li, S., Pan, G., 2019. Numerical modelling of dynamic responses of a floating offshore wind turbine subject to focused waves. Energies 12 (18), 3482.